Title	Density functional theory-based studies on precious metal-free surfaces as alternative catalysts for green energy applications : Carbon nanotubes and copper oxide
Author(s)	Moreno, Joaquin Lorenzo Valmoria
Citation	大阪大学, 2015, 博士論文
Version Type	VoR
URL	https://doi.org/10.18910/53964
rights	
Note	

Doctoral Dissertation
博士論文

Density functional theory-based studies on precious metal-free surfaces as
alternative catalysts for green energy applications:
Carbon nanotubes and copper oxide
（密度汎関数理論によるグリーンエネルギー技術に向けた貴金属フリー触媒に
関する理論的研究：カーボンナノチューブと酸化銅）

Joaquin Lorenzo Valmoria Moreno
ホワキン　ロレンゾ　ヴァレモリア　モレノ

July 2015

Department of Applied Physics
Graduate School of Engineering
Osaka University
大阪大学大学院
精密科学 ・ 応用物理学専攻

Abstract

Many catalytic reactions utilize late transition metals such as platinum, rhodium, and palladium. These include oxidation and reduction processes in devices for "green energy" applications, e.g. the oxygen reduction reaction (ORR) in the proton exchange membrane fuel cell (PEMFC) and NO reduction and CO oxidation in the three-way catalytic converter for automotive exhausts. However, the aforementioned metals are known to be expensive and limited in supply – thus, they are often referred to as precious metals. The need to lower costs by reducing the consumption of these precious metals has necessitated the search for alternative precious metal-free catalysts.

The interaction of simple gas molecules, e.g. oxygen, nitrogen oxide, and carbon monoxide, with precious metal-free surfaces is studied using density functional theory-based calculations to contribute to the understanding of the oxidation and reduction reactions. In the first part, the possibility of copper oxides as potential catalyst material in the three-way catalytic converter, wherein NO_x, CO, and hydrocarbons are converted into less hazardous gases, is explored. In the second part, the interaction of oxygen with single-walled carbon nanotubes (SWCNTs) and graphene is investigated for potential use as a catalyst for oxygen reduction in the PEMFC.

NO reduction is believed to be the rate limiting step in the catalytic converter. Therefore, the dissociation of NO on $Cu_2O(111)$ and $CuO(110)$ surfaces was first investigated. The NO molecule strongly adsorbs on Cu-terminated $CuO(110)$ and $Cu_2O(111)$ surfaces and have shown better reactivity than $Cu(111)$ surface for NO dissociation. The strong electron transfer from the unsaturated Cu atoms to the NO molecule accounted for the easier dissociation of the NO molecule on the Cu-terminated surfaces. The interaction of subsurface O atoms caused the shift of the d-band of the unsaturated Cu atoms, thus providing more occupied states near the Fermi energy. This allowed the excellent hybridization between the d states of the unsaturated Cu atoms and anti-bonding $\pi*$ states of the NO molecule, as evidenced by the strong back-donation.

Next, CO oxidation was investigated. The CO molecule adsorbs on the Cu-terminated copper oxide surfaces and reacts with a coadsorbed O adatom, forming an adsorbed CO_2 molecule. Similar with the case of NO reduction, the unsaturated Cu atoms on the surfaces are responsible for the good reactivity of the copper oxides with CO. Comparing the results on copper oxide with the benchmark catalyst, rhodium, the copper oxide surfaces provide lower activation energy barrier for both NO reduction and CO oxidation. Thus, it can be concluded that copper oxides are indeed promising as precious metal-free catalysts for the purification of automotive exhausts.

The interaction of oxygen with SWCNTs was investigated by looking at the effects of surface curvature, as well as that of Fe-filling inside the SWCNTs. A comparative study on the interaction of oxygen with SWCNTs and graphene was conducted. SWCNTs used in the study have chiralities of (3,3), (5,0), (5,5) and (8,0), listed in order of decreasing surface curvature. The effect of curvature on the adsorption of atomic and molecular oxygen on SWCNTs and graphene was analyzed by investigating its adsorption energetics, structural properties, and charge distributions. The oxygen atom is strongly chemisorbed on the bridge site of the SWCNTs and the adsorption energy increases with greater curvature. The adsorption is accompanied by a large electron transfer from the carbon atoms in the bridge site to the adsorbed oxygen atom, and is likewise enhanced by greater curvature. The effect of surface curvature on the molecular adsorption of oxygen was then investigated. The oxygen molecule interacts weakly with SWCNTs and the interaction is mainly due to van der Waals forces. Greater surface curvature also enhances the adsorption energy. The energy barriers for O_2 dissociation are reduced with increasing curvature. The sp^3-like hybridization of the carbon atoms in SWCNTs with large curvature accounts for the stronger interaction with oxygen. A greater degree of depletion of antibonding π^* states is also observed for larger curvatures, resulting in larger HOMO-LUMO gaps, which is consistent with the enhanced adsorption energies. The interaction of oxygen and H_2O_2 with SWCNTs filled with Fe was also studied. While the presence of Fe inside SWCNTs results in a slightly weaker oxygen adsorption, the energy barrier for O_2 dissociation is reduced and Fe-filled SWCNTs are resistant to oxidation from H_2O_2 poisoning. It should be noted that H_2O_2 selectively destroys semiconducting SWCNTs due to the hole-doping effect induced by H_2O_2 interaction. With the exception of ultra-small diameter SWCNTs (~4Å), the presence of Fe inside SWCNT changes the electronic property of the SWCNTs to metallic, thus preventing the degradation of the material due to H_2O_2 poisoning and allowing oxygen reduction reactions that involve peroxide intermediates. Therefore, the presence of Fe improves the catalytic potential of SWCNTs due to the reduced O_2 dissociation energy barrier and resistance to H_2O_2 poisoning.

In summary, DFT-based calculations were conducted to study the interaction of simple gas molecules (such as O, NO, and CO), with precious metal-free surfaces. A detailed analysis of the NO reduction and CO oxidation processes on Cu(111), CuO(110), and Cu_2O(111) surfaces was obtained. The excellent reactivity of the copper oxides with both NO and CO make them good catalysts for NO reduction and CO oxidation, and may be of potential use as an alternative catalyst for the three-way catalytic converter. The effects of surface curvature and the presence of Fe on the interaction of oxygen with SWCNTs were explained as well. By combining the effect of surface curvature and Fe-filling, the reactivity of SWCNTs with oxygen can be increased and its durability towards H_2O_2 poisoning improved, thus opening numerous possibilities for designing CNT-based precious metal-free catalysts for oxygen reduction in the PEMFC.

Contents

List of Figures

List of Tables

Chapter 1

Introduction

Modern society is greatly dependent on catalysis, i.e. the production of most industrially important chemicals involves catalysis. Catalysis is relevant to a wide range of fields, but most noteworthy is its significance to environmentally friendly applications, e.g. the catalytic converter in automobiles, and alternative energy sources such as fuel cells. Thus, research into catalysis has become a major field in applied science and involves many areas of chemistry and physics, in particular surface and materials science. Catalytic reactions are preferred especially in these so-called "green energy" applications due to the reduced amount of energy consumed and waste generated, as opposed to conventional stoichiometric reactions wherein all reactants are consumed and unwanted side products can be formed. In this Dissertation, potential alternative precious metal-free catalysts for various "green energy" applications are investigated.

In this introductory chapter, the role of surfaces as catalysts and the overview of the research approach are presented to provide a general picture of the conduct of this study.

1.1   Role of Surfaces as Catalysts

Catalysis is the increase in the rate of a chemical reaction due to the participation of an additional substance known as a catalyst. A catalyst speeds up the reaction without itself being consumed in the overall process, thus only tiny amounts are required in most cases. It works by providing an alternative pathway to increase the rate of reaction to end with the same reaction product, i.e. less free energy is required to reach the transition state, but the total free energy from reactants to products does not change.

Consider a hypothetical exothermic chemical reaction with two reactants, X and Y, resulting in the product Z. Fig. 1.1 shows a generic potential energy diagram showing the effect of a catalyst to this particular reaction. The presence of the catalyst allows a different reaction path (shown in red) with lower activation energy, E_a. The final result of the reaction remains the same, as indicated by the same change in free energy, ΔG, with or without the catalyst.
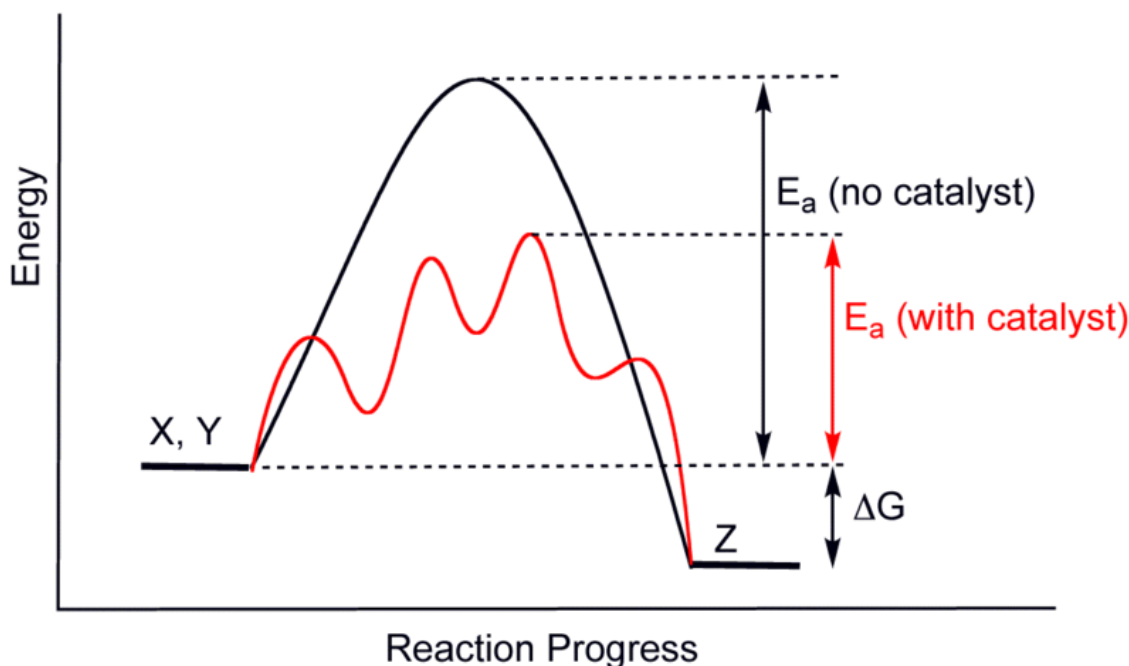
Figure 1.1: Generic potential energy diagram showing the effect of a catalyst in a hypothetical reaction X + Y → Z.

Surfaces play a major role in heterogeneous catalysis, i.e. the catalysts and reactants have different phases. Reactions on surfaces normally involve adsorption and desorption steps, especially those that occur at the solid-gas interface. Experimentally, it is possible to observe such reactions in real space via scanning tunneling microscopy, provided that the time scale of the reaction is in the correct range. [1] The most common types of catalytic surface reactions include simple decomposition, e.g. dissociative adsorption, and bimolecular reactions, e.g. CO oxidation on platinum. Diverse mechanisms can take place for bimolecular reactions, such as the Langmiur-Hinshelwood mechanism, which will be discussed in further detail in Chapter 2.

1.2   Precious Metal Catalysts

The chemical nature of catalysts is as diverse as catalysis itself, although some generalizations can be made. Brönsted acids are likely to be the most widely used catalysts, e.g. hydrochloric and sulfuric acids. Multifunctional solids often are catalytically active as well, e.g. metal oxides, graphitic carbon, nanotubes, and nanoparticles. Likewise, transition metals are used in redox reactions. Many catalytic processes, however, require late transition metals such as palladium, platinum, gold and rhodium. Since these metals are known to be expensive and limited in supply, they are often referred to as precious metals.

One of the most popular and environmentally significant processes that require precious metal catalysts is the catalytic converter. It is a vehicle emissions control device that converts toxic pollutants in exhaust gas to less toxic substances by catalyzing a redox reaction, and is widely used in internal combustion engines fueled by either gasoline or diesel. The technology currently available is called three-way catalytic converters, i.e. it does three simultaneous tasks:

1.   Reduction of nitrogen oxides to nitrogen and oxygen: $2NO_x \rightarrow xO_2 + N_2$
2.   Oxidation of carbon monoxide to carbon dioxide: $2CO + O_2 \rightarrow 2CO_2$
3.   Oxidation of unburnt hydrocarbons (HC) to carbon dioxide and water:
      $C_xH_{2x+2} + [(3x+1)/2]O_2 \rightarrow xCO_2 + (x+1)H_2O$
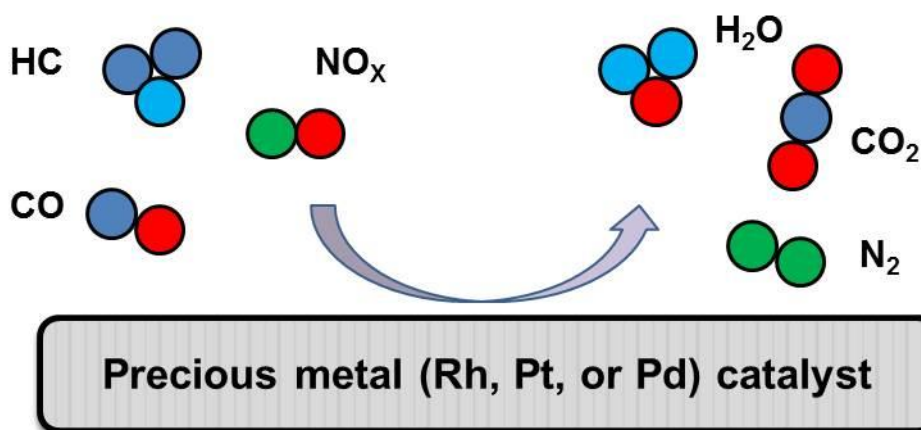
Figure 1.2: Schematic diagram of the three-way catalytic converter, wherein nitrogen oxides (NO_x), carbon monoxide (CO), and hydrocarbons (HC) are converted into less toxic substances such as nitrogen gas (N_2), carbon dioxide (CO_2), and water (H_2O).

The catalyst used for the three-way catalytic converter is most often a combination of the precious metals rhodium, platinum, and palladium [2]. A schematic diagram of how a three-way catalytic converter works is shown in Fig. 1.2.
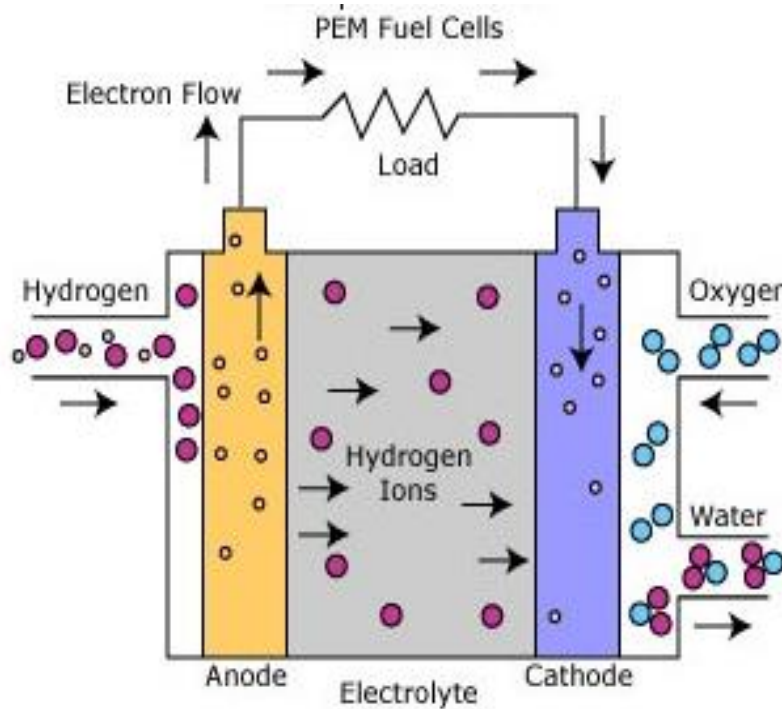
Figure 1.3: Schematic diagram of a proton exchange membrane fuel cell, wherein the electrochemical reaction of hydrogen and oxygen to form water is utilized to generate electrical energy.

Another device that utilizes precious metal catalysts is the proton exchange membrane fuel cell (PEMFC). A PEMFC transforms the chemical energy liberated during the electrochemical reaction of hydrogen and oxygen to electrical energy, as opposed to the direct combustion that produces thermal energy. Hydrogen fuel is delivered to the anode side of the membrane electrode assembly (MEA) where it is catalytically split into protons and electrons in an oxidation half-cell reaction that is more known as the hydrogen oxidation reaction (HOR). The newly formed protons permeate through the polymer electrolyte membrane while the electrons travel along an external load circuit to the cathode side of the MEA, creating the current output of the fuel cell. Meanwhile, oxygen is delivered to the cathode side (most often just atmospheric oxygen) where it reacts with the permeating protons and the arriving electrons from the external circuit to form water. This reduction half-cell reaction is known as the oxygen reduction

reaction (ORR). The entire process can be summarized as follows.

1. At the anode, hydrogen oxidation reaction: $H_2 \rightarrow 2H^+ + 2e^-$
2. At the cathode, oxygen reduction reaction: $\frac{1}{2}O_2 + 2H^+ + 2e^- \rightarrow H_2O$
3. Overall reaction: $H_2 + \frac{1}{2}O_2 \rightarrow H_2O$

Platinum is by far the most effective catalyst and nearly all current PEMFCs use platinum particles on porous carbon supports to catalyze both HOR and ORR [3]. A schematic diagram of how a PEMFC works is shown in Fig. 1.3.

1.3   General overview of research approach

Atmospheric pollution is one of the main environmental concerns of our society at present. Pollutant emissions from mobile sources such as vehicles, trains and airplanes account for more than half of all pollutants in the atmosphere. One main reason is the continuing dependence on fossil fuels, which when combusted emit pollutant gases such as nitrogen oxides (NO_x), carbon monoxide (CO), and hydrocarbons (HC). Such pollutant emissions give rise to smog and acid rain which have adverse effects not just on the welfare of humankind, but also to the environment in general. Thus, limiting or totally eradicating these pollutant emissions is needed to address this concern.

The three-way catalytic converter and PEMFC discussed in the previous section are both viable solutions to atmospheric pollution. The three-way catalytic converter can be used to purify exhaust emissions, whereas the PEMFC can totally eradicate pollutant emissions by replacing conventional combustion engines that rely on the dwindling global supply of fossil fuels. However, both of them rely on precious metals as catalysts for their respective processes and thus, their use has been limited. The need to find alternative precious metal-free catalysts has therefore become one of the major trends in catalysis research and is also the main focus of this dissertation.

Despite major advancements in experimental methods, most experimental techniques in discovering potential catalysts for particular reactions involve combinatorial and intuitive methods that are time-consuming and not cost efficient, because success is not guaranteed. However, recent developments in computational techniques, coupled with the rapid progress in terms of efficiency and computational capability of supercomputers have allowed the possibility

of designing catalysts at the atomic level that promote the desired selectivity and catalytic activity. Such computational techniques employ density functional theory (DFT) calculations. Basically, DFT is a computational quantum mechanical modelling method that is used to investigate the ground state electronic properties of many-body systems. In this theory, the ground state properties of such quantum mechanical systems are functionals (i.e. function of a function) of the electron density. A more detailed discussion about DFT is presented in the Appendix section.

In this Dissertation, DFT-based calculations are employed to further understand the catalytic processes that take place in the three-way catalytic converter and PEMFC. In Chapter 2, the reduction of NO and oxidation of CO are discussed, with a copper-based material as a potential precious metal-free catalyst for the three-way catalytic converter. Then in Chapter 3, the adsorption and dissociation of oxygen is discussed, with a carbon-based material as another potential precious metal-free catalyst for the ORR in the PEMFC.

Chapter 2

Purification of Automotive Exhausts: Copper Oxide Surfaces

2.1   Introduction

The reduction of nitrogen oxide (NO) and oxidation of carbon monoxide (CO) are basic heterogeneous catalytic reactions of fundamental significance. They usually occur on transition metal and metal oxide surfaces. In recent years, these reactions have gained more attention due to the need to control atmospheric pollution. Both reactions are key processes that take place in three-way catalytic converters that are used to suppress pollutants in automobile exhaust emissions. Several transition metals (such as Rh, Pd, and Pt) are known to be active catalysts for both reactions [2]. However, their high cost has been a hindrance to the widespread use of three-way catalytic converters. Thus, an inexpensive and more readily available material without sacrificing catalytic performance is needed.

First of all, understanding the mechanisms behind these reactions is of utmost importance. Both reactions have been widely studied in the literature [2, 4-15]. It is generally believed that NO reduction is driven by a simple dissociation mechanism on a catalytic surface, involving only a couple of steps: (i) NO adsorption on the surface, and (ii) NO dissociation into N and O adatoms on the surface [4-5]. Breaking the N-O bond requires a large amount of energy, thus making it the rate-limiting step in the catalytic converter. In contrast, CO oxidation is believed to follow a Langmuir-Hinshelwood mechanism, i.e. the reactants in a bimolecular reaction both adsorb on a surface then the adsorbed molecules undergo a bimolecular reaction. There are three proposed elementary steps: (i) CO adsorption on the surface, (ii) O_2 dissociation into O adatoms on the surface, and (iii) CO + O $\rightarrow$ CO_2 reaction on the surface [6]. In the case of three-way catalytic converters, O adatoms on the surface can also be provided by NO dissociation.

The objectives of this chapter can be summarized in the graphic given by Fig. 2.1. Both NO reduction and CO oxidation are driven by precious metal catalysts. The aim of the study is to find an alternative precious metal-free catalyst material than can catalyze both reactions.
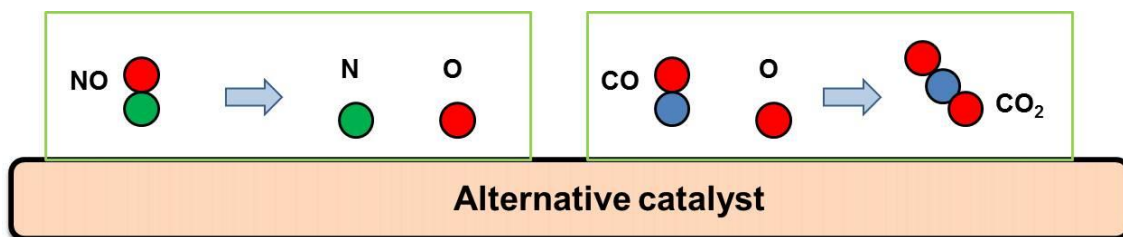
Figure 2.1: The objectives of this chapter are summarized as follows: to find an alternative precious metal-free catalyst that can catalyze both NO reduction and CO oxidation reactions shown in the green boxes.

2.2   Why copper based catalysts?

Among the other available transition metals, copper seems to be the most promising as a catalyst for both NO reduction and CO oxidation. Earlier research has suggested that Cu is a suitable candidate for improving the catalytic properties of precious metals such as Rh and Pd while simultaneously reducing the cost of production. Improved catalytic activity for CO adsorption has been observed in PdCu bimetallic crystals [16]. Also, under laboratory conditions, RhCu catalyst was found to perform better than industrial Rh catalysts for both CO oxidation and NO reduction [17-18]. Moreover, Cu thin films [19] and low index surfaces [20-21] have exhibited reactivity towards NO adsorption, although a DFT-based study concluded that NO dissociation is activated [22]. Nevertheless, it was proposed that the presence of Cu on precious metals such as Rh would promote NO dissociation. The activation barrier was reduced by about 0.4 eV due to the presence of Cu on Rh (111) as shown in Fig. 2.2. Recently, a study on the dissociation of NO and NO_2 on Cu(111) with and without the presence of coadsorbed N and O atoms on the surface was carried out. It was suggested that NO dissociation on the Cu surface is enhanced by the presence of an N atom while its reactivity is reduced by a coadsorbed O atom [23].

Similarly, another recent DFT study investigated CO oxidation on bimetallic RhCu(111) surface and predicted a reduced energy barrier compared with CO oxidation on pure Rh(111) surface [24]. Furthermore, copper oxides with metal oxide support have also been investigated

experimentally for catalytic CO oxidation [25-27]. Conversion rates of up to 99.5% for CO to CO_2 conversion have been observed. The proposed mechanism is a redox cycle involving the reduction of Cu^{2+} to Cu^+ by CO, as detailed in Fig. 2.3 [27]. The reduced Cu^+ then reacts with supplied O_2 from the air (or with NO in the case of the three-way catalytic converter) to form CO_2.

(a)

(b)
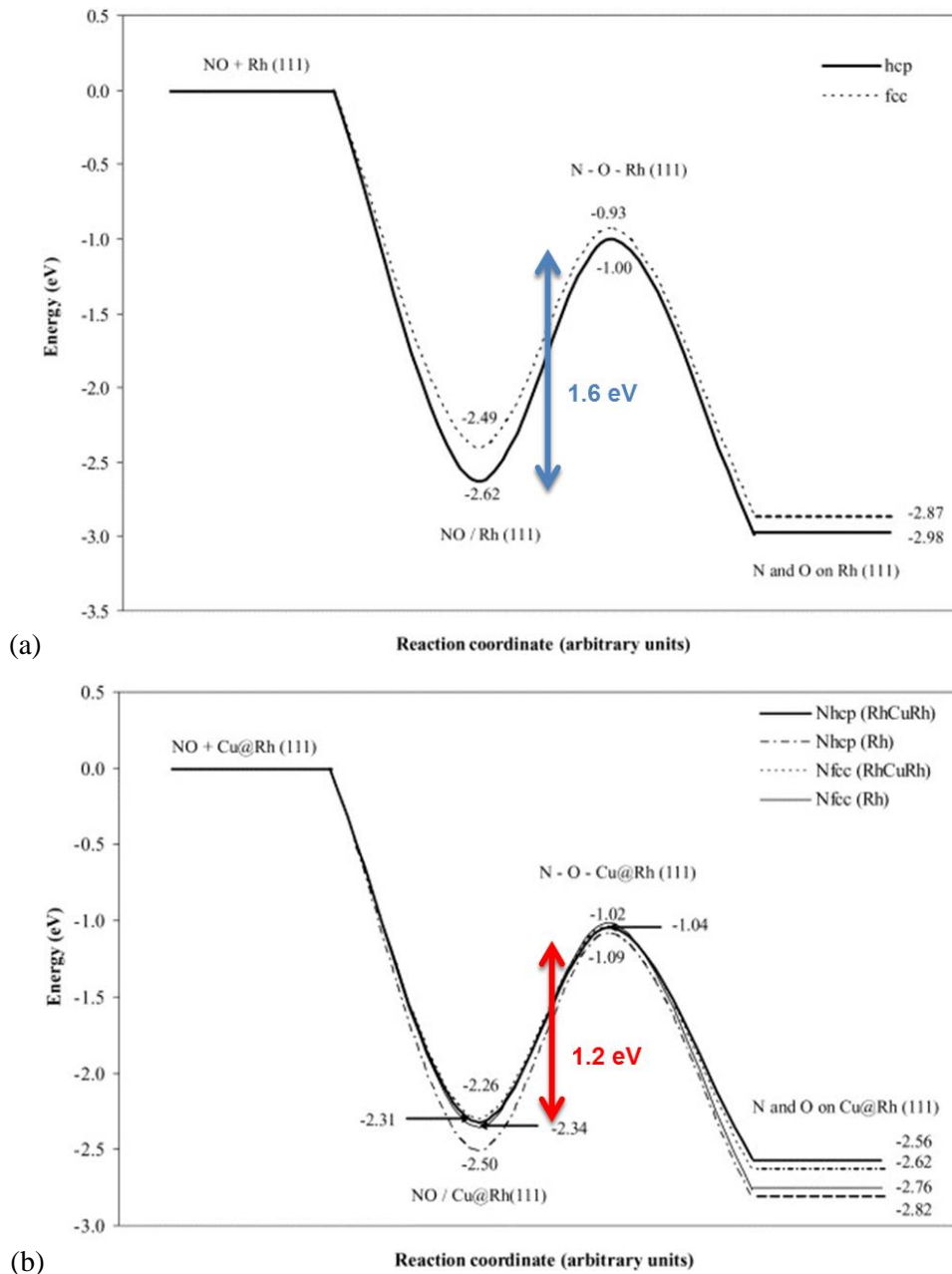
Figure 2.2: Calculated minimum reaction pathway of NO dissociation on (a) Rh (111) and (b) Cu@Rh (111) taken from Ref. 22. Inset blue and red arrows show the least activation energy barrier for Rh (111) and Cu@Rh (111) respectively.
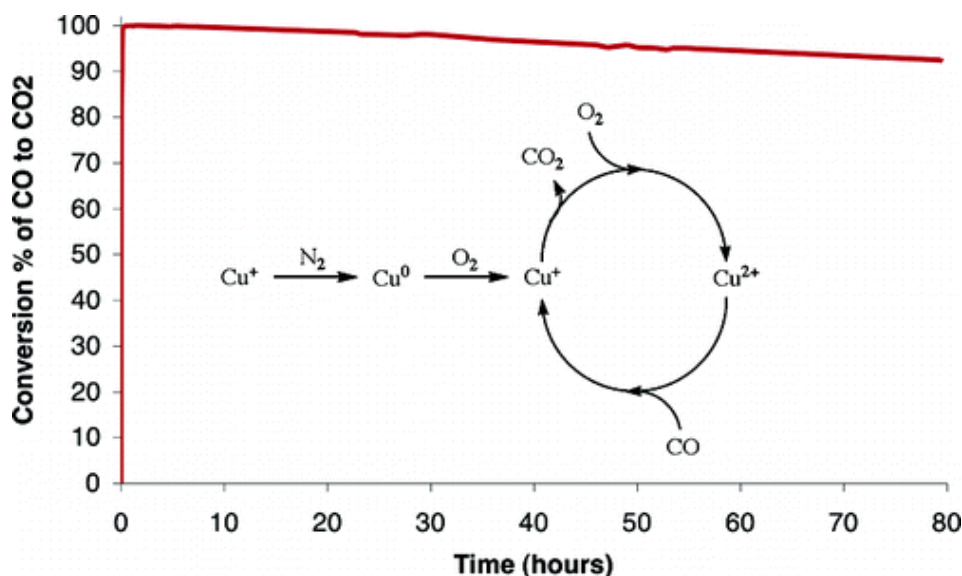
Figure 2.3: Conversion rate of CO to CO_2 on copper oxide nanoparticles, shown as a function of time elapsed, taken from Ref. 27. The inset shows the proposed mechanism of CO oxidation, involving the reduction of Cu^{2+} to Cu^+.

Experimental results from a research collaborator also show the potential of copper oxides. A high NO_x conversion rate of 98.3% was obtained on $Cu_2O(111)$ under a reducing atmosphere, whereas only 5.7-23.6% was attained for other oxide surfaces. Thus all previous work supports the high reactivity of Cu_2O surface towards NO_x reduction. In addition, CuO nanocrystals have recently gained attention for its interesting catalytic properties [28-30]. In this study, a detailed investigation on NO reduction and CO oxidation on CuO(110) surface is performed. The (110) facet was chosen due to the presence of active sites in its Cu-terminated surface [31]. Moreover, X-ray diffraction characterization of CuO thin films have also shown that one of the highest observed peaks corresponds to the (110) facet [33].

In this chapter, copper oxides are further studied and compared with pure copper. Both Cu^+ and Cu^{2+} oxides, i.e. CuO(110) and $Cu_2O(111)$ surfaces are considered. The results and conclusions obtained in this work will bring us closer to the goal of realizing a cheap and efficient precious metal-free exhaust catalyst for NO reduction and CO oxidation.

2.3   Computational model

The atomic and electronic structures of the adsorbate-substrate systems are obtained using

calculations based on density functional theory [32-33] and are performed using the Vienna ab initio simulation package (VASP) [34-35]. The theoretical background and implementation of this method are discussed in the Appendix. The electron-ion interaction is treated using the Projector Augmented Wave (PAW) method [36]. The Kohn-Sham (KS) one-electron valence states are solved in a periodic system by expanding the wave function in a basis of plane waves with an energy cutoff of 400 eV. The exchange-correlation energy is based on the generalized gradient approximation (GGA) using the Perdew-Burke-Ernzerhof (PBE) functional [37-38]. To account for possible effects of long-range dispersion or van der Waals interactions, the DFT-D2 method of Grimme [39] is used to introduce empirical corrections for dispersion interactions to the DFT calculations.

Figure 2.4: Schematic ball-and-stick representation of a monoclinic CuO unit cell in bulk phase. The blue spheres represent Cu atoms and red spheres represent O atoms.

Table 2.1: Comparison of calculated structural parameters for CuO with experimental results obtained from Ref. 40. The Cu-O bond lengths are given by d_1 and d_2, as shown in Fig. 2.4.

Parameter	Calculated	Experimental	% Difference
d_1	1.972 Å	1.961 Å	0.56%
d_2	1.968 Å	1.964 Å	0.71%
O-Cu-O angle	82.14°	84.32°	2.62%

Cupric oxide (CuO) has a monoclinic structure with space group C2/c1 (a = 4.690 Å, b = 3.420 Å, c = 5.131 Å and β = 99.540°) [40]. The unit cell in bulk phase is shown in Fig. 2.4. The calculated structural parameters are in good agreement with experimental results [41], as shown in Table 1. The CuO(110) surface is represented by a periodically repeated slab of nine atomic layers in a 2x2 unit cell., which can be terminated by a layer of Cu atoms (Cu-terminated) or a layer of Cu and O atoms with twice as much O atoms (CuO_2-terminated). Each slab is separated by ~25 Å of vacuum to avoid interaction between adjacent slabs in the repeated supercell. Surface relaxation is considered by optimizing the two topmost layers of the surface and keeping the other layers in their bulk parameters. Most of the surface relaxation occurred along the z-direction as the inter-layer distance between the topmost and second layer showed some contraction for both surface terminations. Between the second and third layers however, no noticeable change in the inter-layer distance was observed (bulk parameters are maintained). The Cu-terminated surface contracted by 0.11 Å while the CuO_2-terminated surface contracted by 0.08 Å, which is consistent with a previous theoretical study [31].
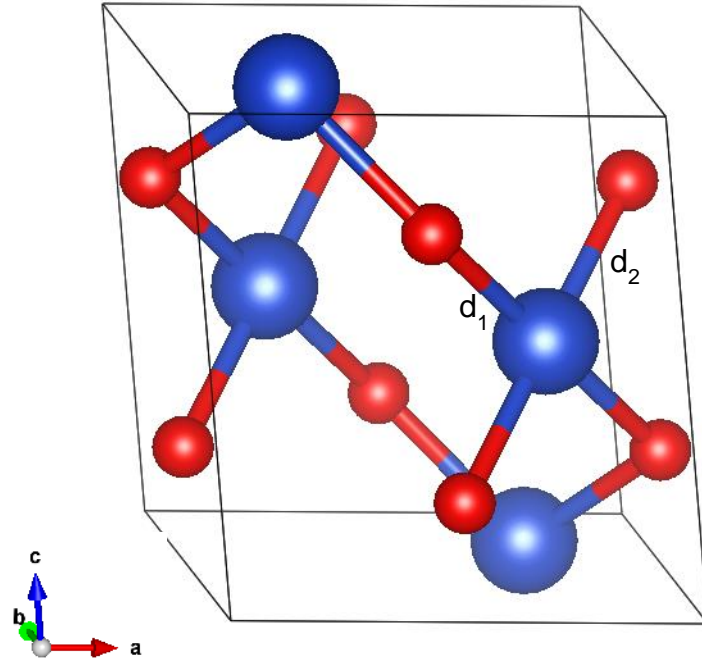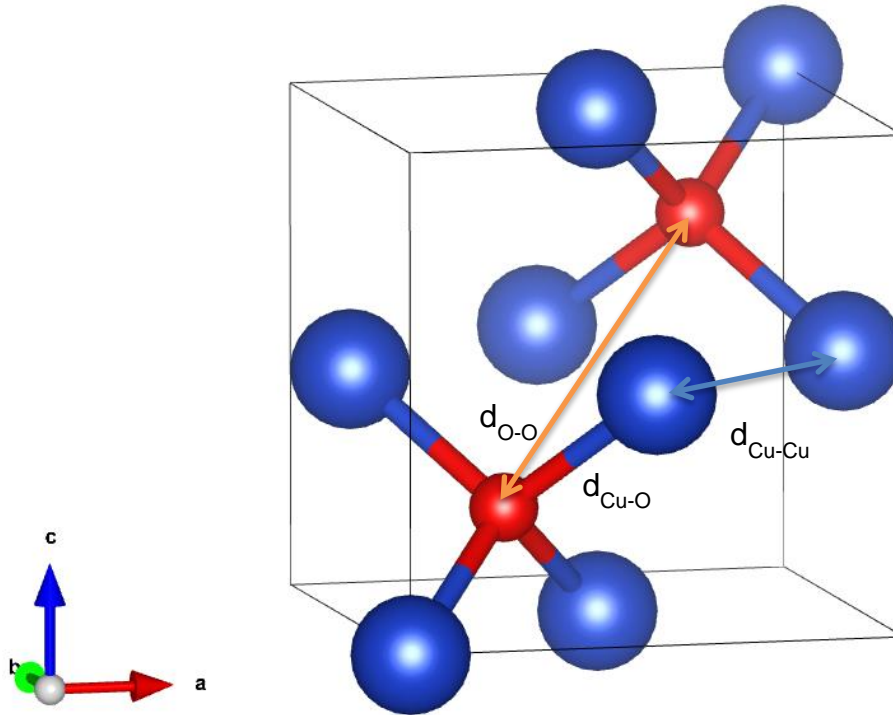

Figure 2.5: Schematic ball-and-stick representation of a cubic Cu_2O unit cell in bulk phase. The blue spheres represent Cu atoms and red spheres represent O atoms.

On the other hand, cuprous oxide (Cu_2O) has a cubic structure, the cuprite (natural Cu2O mineral) type, of space group T_h^2-Pn3 or O_h^4-Pn3m ($a = 4.27$ Å). The unit cell in bulk phase is shown in Fig. 2.5. The calculated structural parameters are in good agreement with experimental results [42], as shown in Table 2. The Cu_2O(111) surface is represented by a periodically repeated slab of nine atomic layers in a 2x2 unit cell., which can be terminated by a layer of Cu atoms (Cu-terminated) or a layer of Cu and O atoms (O-terminated). Each slab is separated by ~25 Å of vacuum to avoid interaction between adjacent slabs in the repeated supercell.

Table 2.2: Comparison of calculated structural parameters for Cu_2O with experimental results obtained from Ref. 42. The bond lengths (or shortest distances) are given by d_{Cu-O}, d_{Cu-Cu}, and d_{O-O}, as shown in Fig. 2.5.

Parameter	Calculated	Experimental	% Difference
d_{Cu-O}	1.838 Å	1.841 Å	0.16%
d_{Cu-Cu}	3.042 Å	3.018 Å	0.79%
d_{O-O}	3.631 Å	3.683 Å	1.53%

For comparison, a pure copper surface is also modelled. The calculated lattice constant for bulk Cu is 3.61 Å, which is in agreement with experimental findings [43]. The Cu(111) surface is represented by a periodically repeated slab of four atomic layers in a 3x3 unit cell. The Brillouin zone is sampled using 6 x 6 x 1 Monkhorst-Pack k-points [44] for all surfaces, the accuracy of which was tested through a convergence test.

The stable geometries and adsorption energies of the adsorbates are determined on different symmetry sites as shown in Fig. 2.6. The climbing image-nudged elastic band (CI-NEB) method [45-46] is used to determine the minimum energy paths for NO dissociation and CO oxidation. The path is identified by using four intermediate images between the initial and final states. The calculations are allowed to converge until the minimum force acting on each atom is 0.03 eV/Å. The transition states are then calculated by obtaining the difference between the maximum value in the minimum energy path and the initial state.
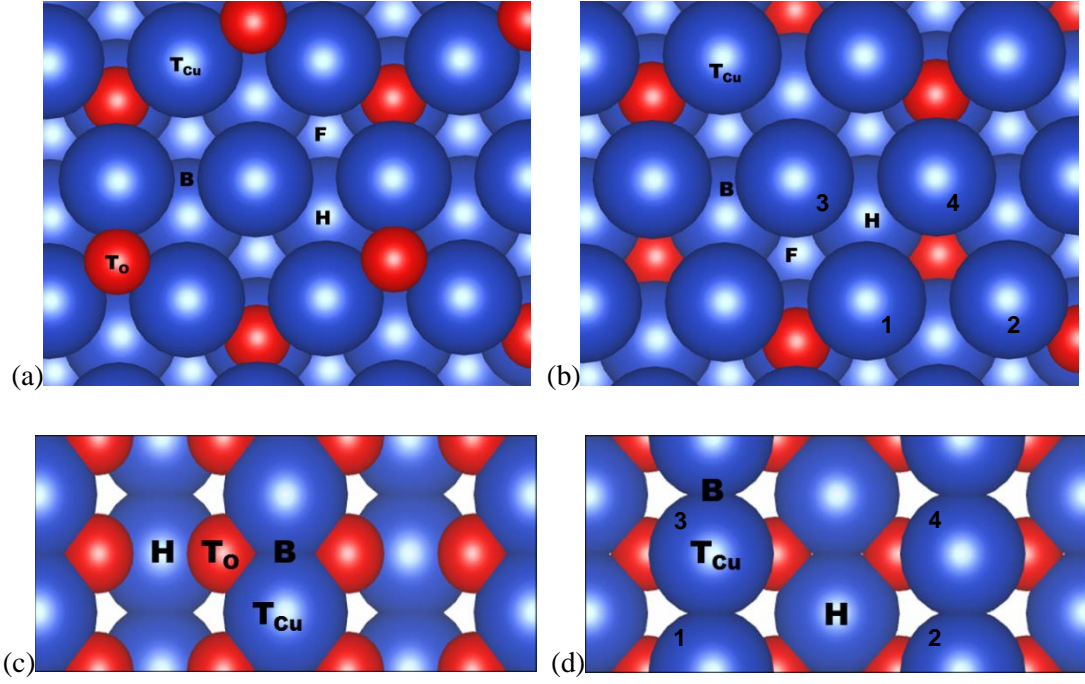
Figure 2.6: Top views of the (a) O-terminated $Cu_2O(111)$, (b) Cu-terminated $Cu_2O(111)$, (c) CuO_2-terminated CuO(110), and (d) Cu-terminated CuO(110) surfaces. The high symmetry sites for NO adsorption are also indicated: T_{Cu} - Cu top site, T_O - O top site, B - bridge site, F - fcc hollow site (Cu_2O only) and H - hcp hollow site (simply hollow site for CuO).

2.4   Adsorption and dissociation of NO

Molecular and dissociative adsorption of NO on Cu(111), $Cu_2O(111)$, and $CuO_2(110)$ surfaces are considered to establish the different possibilities for the interaction of NO on the surfaces. For the molecular adsorption of NO, the adsorption energies on different symmetry sites are calculated using the following equation,

$$E_{ads} = E_{sys} - E_{iso}, \tag{1}$$

where E_{ads} is the adsorption energy, E_{sys} is the calculated total energy of the system, and E_{iso} is the summed energy of the isolated NO molecule and bare surface. This is carried out for different initial configurations for NO adsorption, i.e. perpendicular to the surface with either O-end or N-end interacting with the substrate, in order to distinguish the most stable geometric structure of the NO molecule on the surface.

14

On Cu(111), the most stable structure of the NO molecule is on the fcc hollow site with its axis perpendicular to the surface in an N-end configuration, as shown in Fig. 2.7a. The adsorption energy is 0.920 eV and the distance of NO from the surface is 1.33 Å. The N-O bond length is 1.22 Å, with a minimal elongation compared to the calculated equilibrium bond length of 1.17 Å for the isolated NO molecule in gas phase (in good agreement with the experimental value [47]). These obtained bond lengths are consistent with previous theoretical work [48]. For coadsorbed N and O atoms, the easiest pathway for NO dissociation is when O goes to the next fcc hollow site, as shown in Fig. 2.7c, with adsorption energy of -0.33 eV. Denoting the structures in Fig. 2.7a and Fig. 2.7c as the initial and final configurations, the transition state was obtained using the CI-NEB method. The structure for the transition state is shown in Fig. 2.7b. It has an adsorption energy of 1.03 eV, and the activation barrier to reach the transition state from the initial state is 1.95 eV. Because of the high activation energy barrier and relative instability of the transition state, it can be concluded that NO desorption is more likely to occur on a Cu(111) surface. The observed endothermic reaction of NO on Cu(111) is in agreement with previous studies on the same system [22-23].

(a)   (b)   (c)

Figure 2.7: Stable structures (top view) of (a) molecular adsorption of NO, (b) transition state, and (c) coadsorbed N and O atoms on Cu(111) surface. The blue spheres represent Cu atoms, silver spheres represent N atoms, and red spheres represent O atoms.

For the interaction of NO with $Cu_2O(111)$ surface, both Cu-terminated and O-terminated cases were considered for molecular adsorption. The results are summarized in Table 3. It was determined that NO molecule is most stable at the fcc hollow site, which is far from the O atom in the metal oxide system, with an N-end configuration, as shown in Fig. 2.8a. The adsorption energy is -1.56 eV, the N-O bond length is elongated to 1.28 Å and the distance of NO from the surface is 0.74 Å. These imply that NO is more stable on $Cu_2O(111)$ surface than on Cu(111) surface. The adsorption energies on the O-terminated cases are less stable than the values

obtained for the corresponding Cu-terminated cases. Nonetheless, molecular adsorption of NO is still possible in some adsorption sites on the O-terminated $Cu_2O(111)$ surface, with the fcc hollow site being the most stable as well.

Figure 2.8: Stable structures (top view) of (a) molecular adsorption of NO, (b) transition state, and (c) coadsorbed N and O atoms on $Cu_2O(111)$ surface. The blue spheres represent Cu atoms, silver spheres represent N atoms, and red spheres represent O atoms.

Table 2.3: Adsorption energies (in eV) for NO on different adsorption sites on $Cu_2O(111)$. The values in parentheses indicate the obtained adsorption energies without van der Waals corrections.

Adsorption site	Geometry	Cu-terminated		O-terminated	
T_{Cu}-site	N-end	-1.38	(-1.12)	-0.67	(-0.45)
	O-end	-0.47	(-0.22)	0.15	(0.33)
T_O-site	N-end	-	-	-0.61	(-0.39)
	O-end	-	-	0.21	(0.37)
B-site	N-end	-1.45	(-1.26)	-0.53	(-0.27)
	O-end	-0.61	(-0.40)	0.25	(0.48)
F-site	N-end	-1.56	(-1.29)	-0.98	(-0.72)
	O-end	-0.78	(-0.51)	0.15	(0.33)
H-site	N-end	-1.42	(-1.18)	-0.72	(-0.50)
	O-end	-0.50	(-0.29)	-0.05	(0.18)

For coadsorbed N and O atoms, the easiest pathway for NO dissociation is when O goes to the next fcc hollow site just like in the case of Cu(111), as shown in Fig. 2.8c, with adsorption energy of -1.69 eV. Again, denoting the structures in Fig. 2.8a and Fig. 2.8c as the initial and final configurations, the transition state was obtained using the CI-NEB method. The structure for the transition state is shown in Fig. 2.8b. It has an adsorption energy of -0.40 eV, and the

activation barrier to reach the transition state from the initial state is 1.17 eV. Since the calculated transition state lies below the reference energy, the adsorption energy is sufficient to enable NO dissociation without supplying extra energy to the NO. This is in contrast to the case of NO on Cu(111) and is comparable to the reported dissociation of NO on Rh(111) surface [22].

Finally, for the case of the interaction of NO with CuO(110), the results for molecular adsorption are summarized in Table 4. The NO molecule is most stable on the hollow site of the Cu-terminated CuO(110) surface with its axis oriented perpendicular to the surface in the N-end configuration as shown in Fig. 2.9a. The adsorption energy for the hollow site is -1.78 eV, compared with -1.62 eV for the Cu-top site and -1.57 eV for the bridge site. The N-surface distance is 0.84 Å and the N-O bond length is 1.30 Å. The adsorption energies on the CuO_2-terminated cases are significantly less stable than the values obtained for the corresponding Cu-terminated cases. Nonetheless, molecular adsorption of NO is still possible in some adsorption sites on the CuO_2-terminated CuO(110) surface, with the hollow site being the most stable as well.
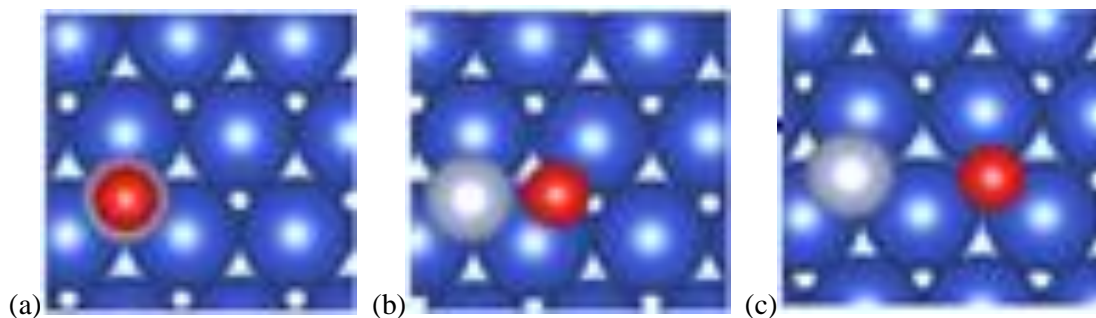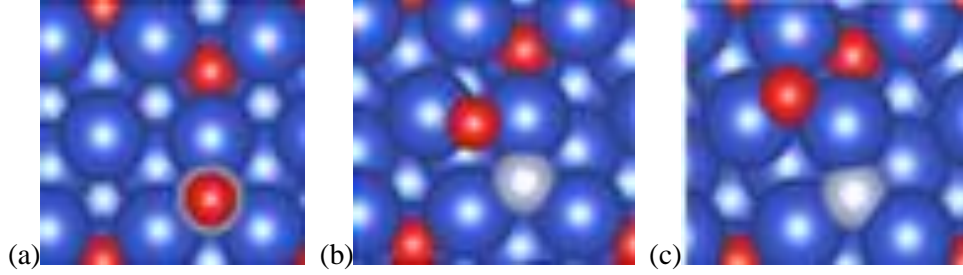

(a)

(b)

(c)
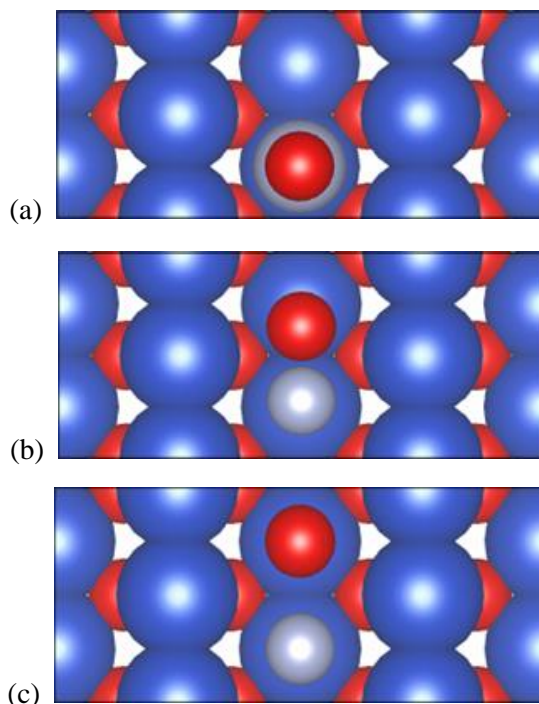
Figure 2.9: Stable structures (top view) of (a) molecular adsorption of NO, (b) transition state, and (c) coadsorbed N and O atoms on Cu-terminated CuO(110) surface. The blue spheres represent Cu atoms, silver spheres represent N atoms, and red spheres represent O atoms.

Table 2.4: Adsorption energies (in eV) for NO on different adsorption sites on CuO (110). The values in parentheses indicate the obtained adsorption energies without van der Waals corrections.

Adsorption site	Geometry	Cu-terminated		CuO_2-terminated	
T_{Cu}-site	N-end	-1.62	(-1.38)	-0.65	(-0.42)
	O-end	-0.45	(-0.21)	0.21	(0.47)
T_O-site	N-end	-		-0.57	(-0.38)
	O-end	-		0.28	(0.53)
B-site	N-end	-1.57	(-1.31)	-0.63	(-0.41)
	O-end	-0.42	(-0.23)	0.26	(0.50)
H-site	N-end	-1.78	(-1.47)	-0.82	(-0.56)
	O-end	-0.59	(-0.36)	0.25	(0.51)

To obtain the easiest pathway for NO dissociation, coadsorbed N and O atoms were calculated with the N atom on the hollow site for both Cu-terminated and CuO_2-terminated surfaces. The O atom was then placed on the other adsorption sites, in addition to the adjacent hollow site. The most stable configuration was when the coadsorbed N and O atoms are on adjacent hollow sites on the Cu-terminated surface as shown in Fig. 2.9c, with an adsorption energy of -1.57 eV. The coadsorbed atoms, however, were found to be unstable on the CuO_2-terinated surface. Thus, the easiest pathway for NO dissociation is when NO is molecularly adsorbed on the hollow site of the Cu-terminated surface with an N-end configuration, and then the O atom goes to the adjacent hollow site. Denoting these as the initial and final states, from Fig 2.9a and 2.9c respectively, the transition state was obtained using the CI-NEB method. The structure for the transition state is shown in Fig. 2.9b. It has an adsorption energy of -0.70 eV, and the activation barrier to reach the transition state from the initial state is 1.07 eV. The N-O distance has elongated to 1.58 Å, but the NO angle with respect to the surface has drastically changed from perpendicular to an almost parallel 5.1°. NO dissociation on CuO is exothermic, with the calculated transition state below the reference energy. The result is very similar to that of NO on $Cu_2O(111)$ surface.

The local density of states (LDOS) of the d orbital of the surface Cu atoms was investigated to explain the reactivity of the copper oxide surfaces when compared with pure copper. The LDOS of the d states of surface Cu atoms in the copper oxides are shifted closer to the Fermi level, as shown in Fig. 2.10. It could be realized that this shifting is a consequence of the interaction of the Cu atoms with the O atoms in the subsurface. In surface analysis, the upshift towards the

Fermi level of the d states characterizes the reactivity of the surface. The electrons in the region of the Fermi level will interact easily with the approaching adsorbate, thus providing better overlapping and hybridization of states. This is true for the surface Cu atoms of the CuO(110) and $Cu_2O(111)$ surfaces, while for Cu(111), since the d states reside far below the Fermi level, the electrons cannot interact well with approaching NO molecules. Therefore, it can be claimed that the higher binding energy of NO on copper oxides is due to this phenomenon.

(a)

(b)

(c)
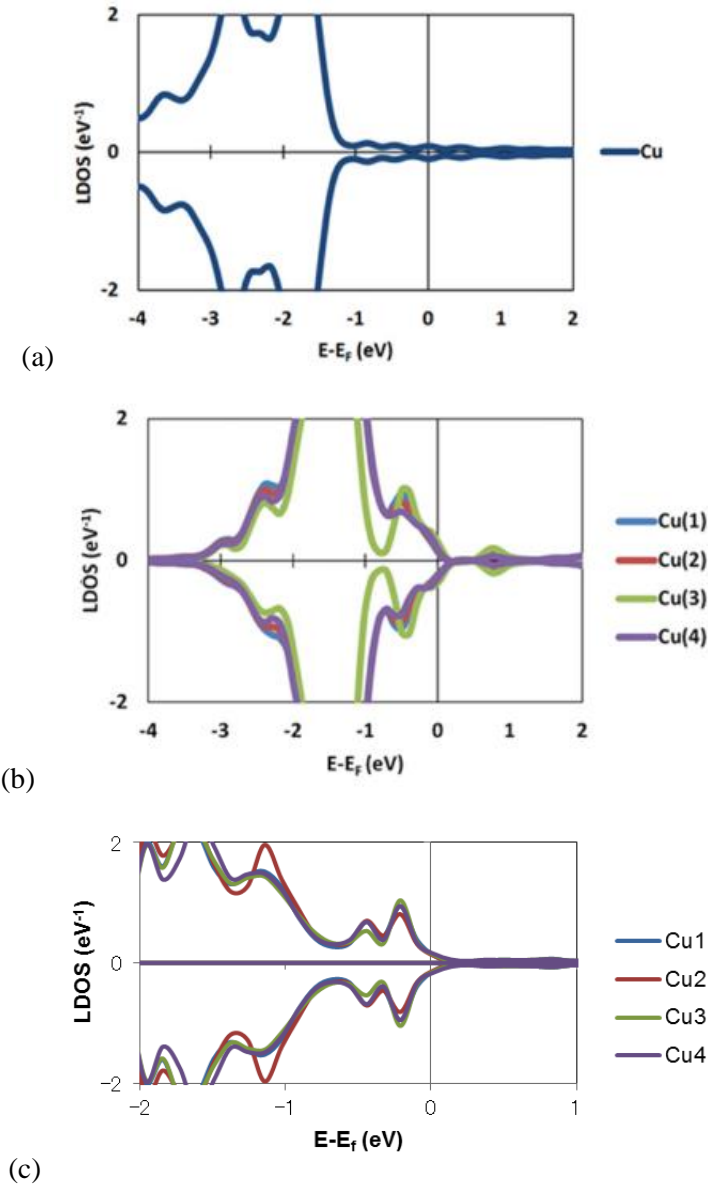
Figure 2.10: LDOS (d orbitals) of surface Cu atoms of (a) Cu(111), (b) $Cu_2O(111)$, and (c) CuO(110). The assigned number of Cu atoms on $Cu_2O(111)$ and CuO(110) corresponds to the four surface Cu atoms in each unit cell in Fig. 2.6. The positive and negative values correspond to spin-up and spin-down electrons, respectively (this applies to all DOS figures).

19

As it was observed that the density of states of the d orbital of the surface Cu atoms in the copper oxides was shifted towards the Fermi level, the charge density distribution of the surfaces in the region along the Fermi level (between -0.5 eV and the Fermi level) was constructed for the case of Cu(111) and $Cu_2O(111)$ for a better comparison of the active sites, as shown in Fig. 2.11. Two dimensional (2D) views of the charge distribution that slices the surface plane are also illustrated. In Cu(111), shown in Fig. 2.11a, along the region of the Fermi level, the charge distribution is localized in its respective atoms as there are a small number of states in the region. The distribution for the case of an O-terminated $Cu_2O(111)$ is also somehow localized, as shown in Fig. 2.11b. In contrast, for Cu-terminated $Cu_2O(111)$, the charge distribution extends along the area of the three-fold site, which is a consequence of the appearance of a peak at about -0.5 eV as identified from the LDOS in Fig. 2.10b. From this, it can be assumed that the three-fold site is an active site of the surface in such a way that charges are present in the site that can participate in the bonding process.
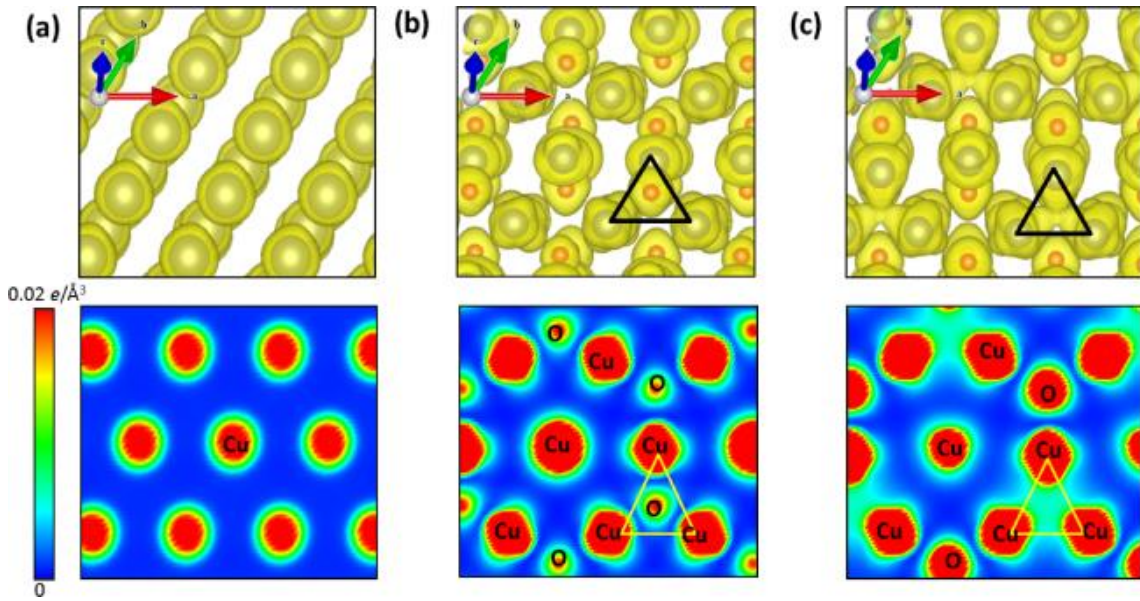
Figure 2.11: Partial charge density distribution and its corresponding 2D view that slices the surface plane of (a) Cu(111), (b) O-terminated $Cu_2O(111)$, and (c) Cu-terminated $Cu_2O(111)$ surfaces evaluated between -0.5 eV and the Fermi energy, with an isosurface value of 0.02 e $Å^3$. The three-fold sites are represented by the triangles.

The local density of states (LDOS) of the d orbitals of surface Cu atoms and the molecularly adsorbed NO before and after the adsorption process are shown in Fig. 2.12. The strong adsorption energy of NO on CuO(110) is explained by the excellent hybridization between the

NO orbitals and Cu d orbitals in the region between -3 eV and the Fermi energy, as can be clearly seen in Fig. 2.12c. Moreover, the elongation of the N-O bond after adsorption can be explained by the strength of the σ bond for the NO molecule. In Fig. 2.12b, the second peak (at around -11.5 eV) corresponds to the 5σ molecular orbital of the NO molecule. After adsorption, the 5σ peak is now at around -7.5 eV, corresponding to a shift towards the Fermi energy and making the sigma bond relatively unstable as compared with NO in gas phase. This weakens considerably the strength of the N-O bond, thus making dissociation easier.
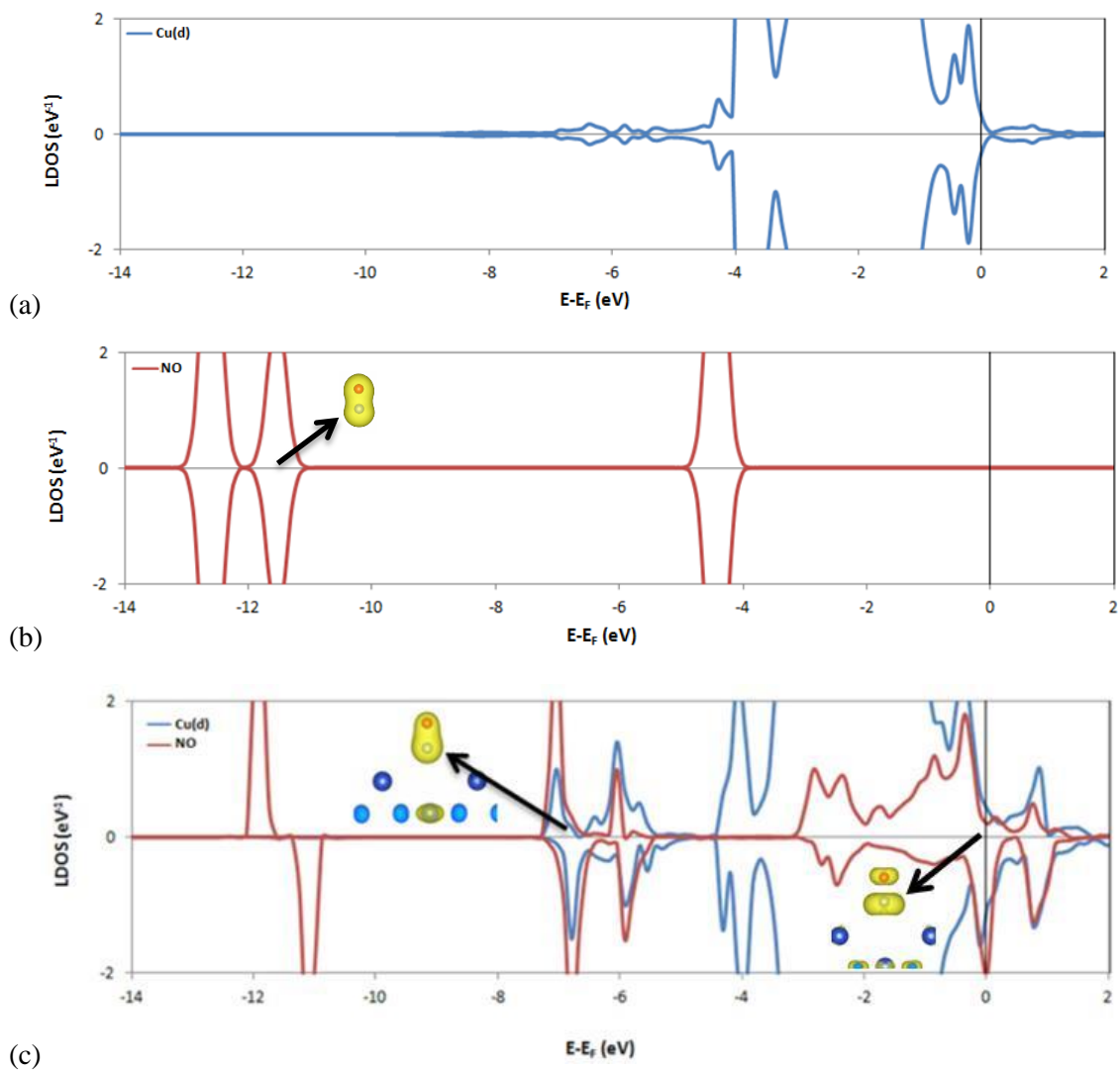
Figure 2.12: (a) LDOS of surface Cu atoms (d states) of a bare CuO(110) surface; (b) LDOS of NO molecule in vacuum; and (c) LDOS of molecularly adsorbed NO and surface Cu atoms (d states) on CuO(110). The insets show the partial charge densities corresponding to the energies indicated by the arrows.

21

The weakening of the N-O bond and dissociation process is explained through the Bader analysis of the charge distribution. After molecular adsorption, the total charge on the adsorbed NO molecule is 11.51|e|, or 4.94|e| in the N atom and 6.57|e| in the O atom. This means the NO molecule has gained 0.51|e| transferred from the surface. Examination of the partial charge density of the NO molecule for the region right below the Fermi level (-0.5 eV to 0 eV) revealed that the extra charge transferred from the surface occupy the previously unoccupied anti-bonding states of NO, as can be seen from the second inset in Fig. 2.12c, and therefore weakens the N-O bond. After dissociation, the total charge of the coadsorbed N and O atoms is 12.45|e|, or 5.71|e| in the N atom and 6.74|e| in the O atom. This corresponds to a gain of 0.94|e| relative to the initial state before dissociation. Thus, a greater charge redistribution between NO and the surface occurs as NO undergoes the dissociation process. In particular, the large charge gain is responsible for the weakening of the N-O bond making the dissociation process easier.

It has been established that the strength of binding between the N and O atoms as a molecule will determine the difficulty of NO dissociation. Table 3 shows a summary of the results pertaining to NO dissociation. The NO molecule exhibits better interaction with the copper oxides as shown by their larger adsorption energies as compared with the pure copper surface. It is evident that the molecularly adsorbed NO on the copper oxides has larger elongation as compared with pure copper, indicating a weaker N-O bond for the adsorbed NO molecule on copper oxides. Fig. 2.13 shows the LDOS of the d orbitals of surface Cu atoms and the molecularly adsorbed NO molecules. The stronger adsorption energy on the copper oxides is reflected in the more pronounced hybridization between NO and the surface Cu atoms in the region between -3 eV and the Fermi energy. However, the 5σ bond for the NO molecule is more stable for the case of the NO-Cu(111) system, and appears at -8 eV (shown by the dashed line for comparison). This sigma bond defines the strength of the N-O bond as established earlier, which is obviously more stable for NO on pure copper compared to NO on the copper oxides. In other words, it is more difficult for O atom to dissociate from the N atom, which is the desired initial step for reduction as shown in the transition states obtained. This explains the high activation barrier obtained for the case of Cu(111).

Table 2.5: Bond length of the adsorbed NO molecule on the surfaces and the corresponding adsorption energies (E_{ads}) and energy barriers (E_B).

Surface	Bond length (Å)	E_{ads} (eV)	E_B (eV)
Cu(111)	1.22	0.92	1.95
Cu-terminated $Cu_2O(111)$	1.28	1.56	1.17
Cu-terminated CuO(110)	1.30	1.78	1.08
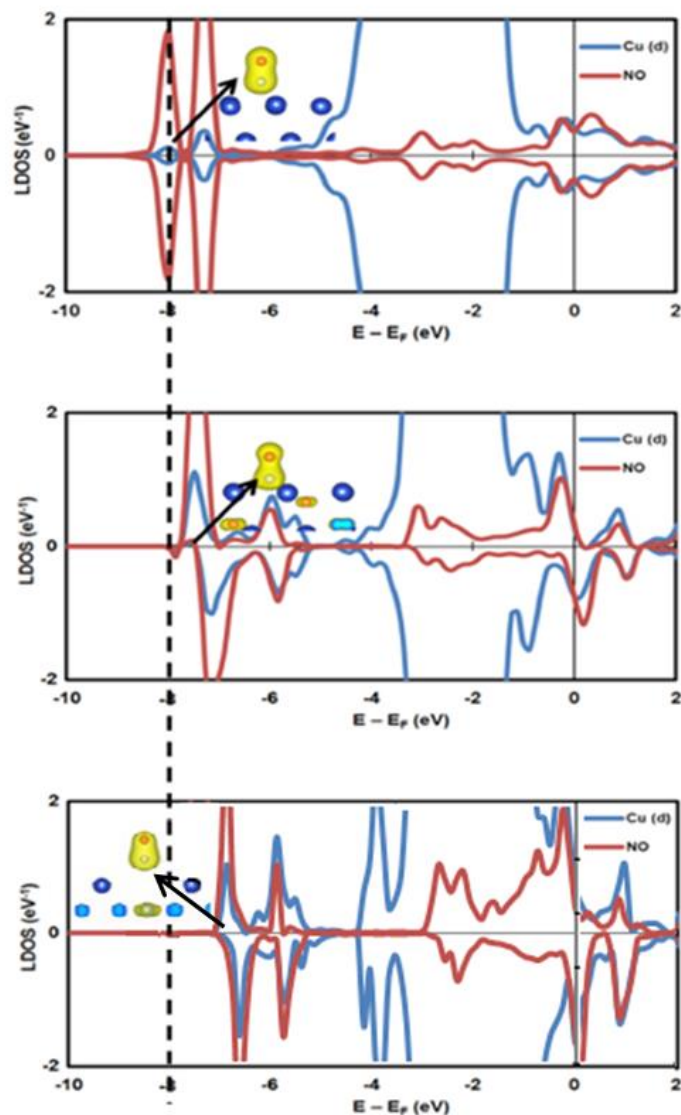
Figure 2.13: LDOS of the adsorbed NO molecules and of the d orbitals of surface Cu atoms of (a) Cu(111), (b) Cu$_2$O(111), and (c) CuO(110). The insets show the charge densities corresponding the the NO sigma bonds as the NO is adsorbed on the surfaces.

Next, the density of states in the transition state is analyzed to fully understand the influence of the surface atoms in the dissociation process. It was pointed out earlier that the transition states for NO on the copper oxides lie below the reference energy and indicates the possibility of dissociation. For the case of Cu(111), the activation barrier is too large, so that NO desorption is more likely to happen than dissociation. Figure 2.14 shows the LDOS of the surface Cu atoms (d orbitals) of both surfaces and of the O and N atoms at the transition state. The figure shows

the hybridization between the Cu atoms and the dissociating N and O atoms on the surface. Overlapping of the states occurs for both cases; however, it is obvious that the degree of overlapping is much greater for the case of the $Cu_2O(111)$ surface, especially in the regions marked by (*) in the figure. This indicates a good binding between the surface and the dissociating N and O atoms. It can be concluded that the effective hybridization of the states is the reason for the stable energy obtained for the dissociation process of NO on $Cu_2O(111)$.
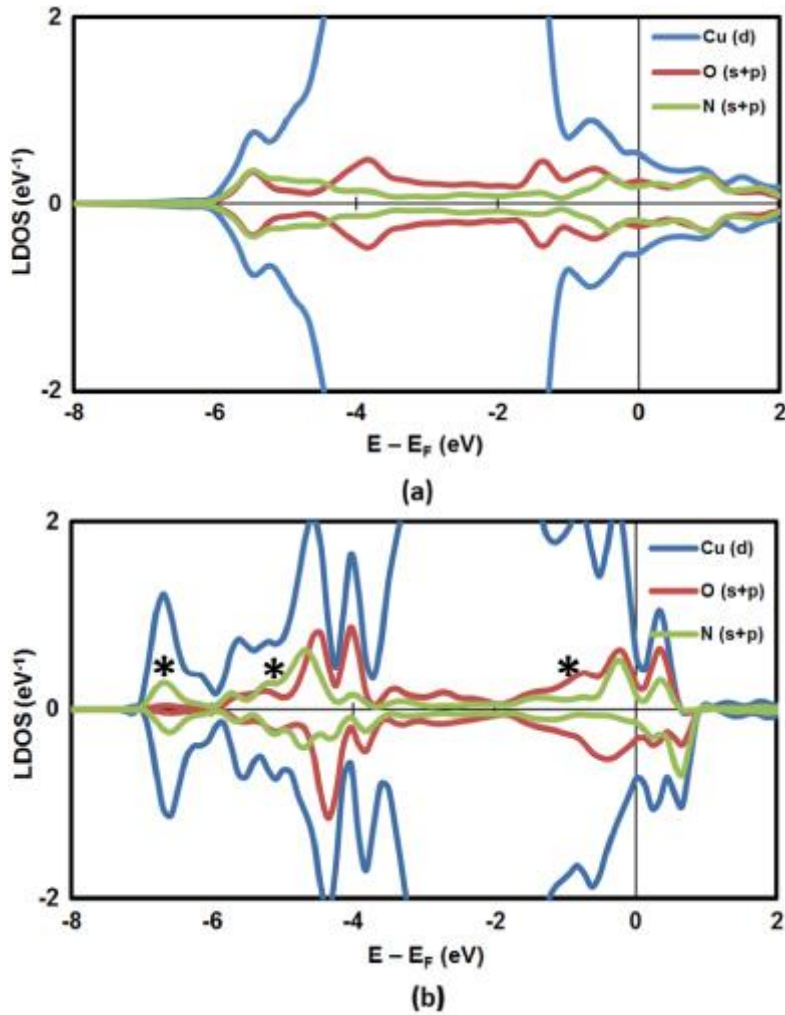
Figure 2.14: LDOS of the dissociating N and O atoms at the transition state and of the d orbitals of surface Cu atoms of (a) Cu(111) and (b) $Cu_2O(111)$. The degree of overlapping is much better for the case of the $Cu_2O(111)$ surface, especially in the regions marked by (*).
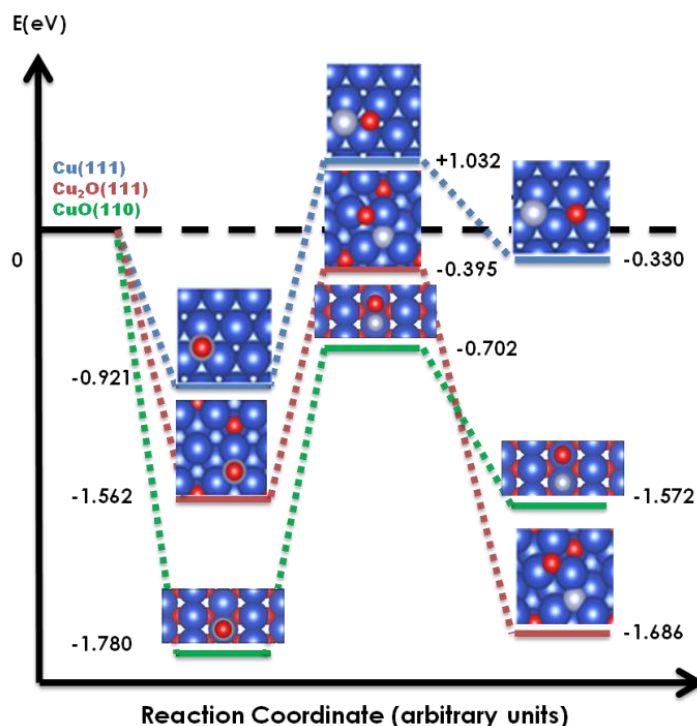
Figure 2.15: Calculated potential energies for the reaction paths of NO dissociation on Cu(111) (blue lines), Cu-terminated $Cu_2O(111)$ (red lines) and Cu-terminated CuO(110) (green lines) surfaces. The insets show the top views of the corresponding geometric configurations in the reaction paths. The blue spheres represent Cu atoms, silver spheres represent N atoms, and red spheres represent O atoms. The horizontal dashed line represents the reference energy, E_{iso} for each system.

To summarize the results for NO reduction, the reaction paths for the dissociation of NO on Cu(111), CuO(110), and $Cu_2O(111)$ are shown in Fig. 2.15. The reaction paths for CuO(110) and $Cu_2O(111)$ surfaces show similar features. Both reactions are exothermic, in contrast with Cu(111) surface. The adsorption energies and energy barriers of the two copper oxides are also similar. Moreover, the transition states lie below reference energy in case of the copper oxides, which is similar to the reaction path of NO dissociation on Rh(111) [22]. The only distinct difference between the copper oxides is that the adsorption energy for the coadsorbed N and O atoms is higher than the adsorption energy for NO molecular adsorption in the CuO(110) surface. This may be favorable for the formation of CO_2 or NCO after interaction with a subsequent adsorbing CO molecule. Furthermore, the activation barrier for both NO reduction and CO oxidation is lower for copper oxides than Rh(111). Therefore, in general, copper oxide is a promising catalyst for NO dissociation, regardless of whether the oxide is cuprous or cupric.

2.5   Oxidation of CO on CuO (110)

As a prelude to the investigation of CO oxidation on CuO(110) after NO dissociation, the molecular adsorption of CO on CuO_2-terminated and Cu-terminated surfaces is first considered to establish the different possibilities for the interaction of CO on CuO(110). The adsorption energies on different symmetry sites are calculated using the same equation given in Eq. 1, where E_{ads} is the adsorption energy, E_{sys} is the calculated total energy of the system, and E_{iso} is the summed energy of the isolated CO molecule and bare surface. This is carried out for different initial configurations for CO adsorption, i.e. perpendicular to the surface with either O-end or C-end interacting with the substrate, in order to distinguish the most stable geometric structure of the CO molecule on the surface. The results are tallied in Table 6.
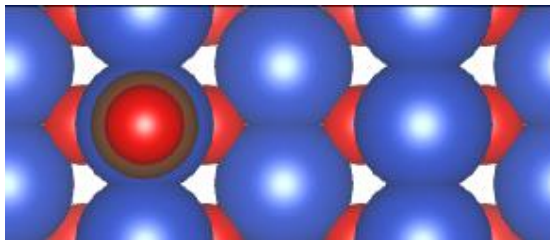
Figure 2.16: Stable structure (top view) for the molecular adsorption of CO on Cu-terminated CuO(110) surface. The blue spheres represent Cu atoms, grey spheres represent C atoms, and red spheres represent O atoms.

The molecular adsorption of CO is most stable on the Cu top site of the Cu-terminated CuO(110) surface with its axis oriented perpendicular to the surface in the C-end configuration as shown in Fig. 2.16. This is in contrast with the molecular adsorption of NO wherein the most stable site is the hollow site. The adsorption energy is -0.84 eV, compared with -0.64 eV for the hollow site and -0.59 eV for the bridge site. The distance between the C atom and the surface Cu atom is 1.93 Å, and the C-O bond length is 1.152 Å, which is elongated compared to the equilibrium C-O bond length for gas phase CO (calculated to be 1.133 Å in vacuum, which is in good agreement with the measured experimental value of 1.128 Å [49]). The adsorption energies on the CuO_2-terminated cases are significantly less stable than the values obtained for the corresponding Cu-terminated cases. In addition, only the Cu top site and bridge site have adsorption energies below the reference energy, albeit barely. Therefore, it can be assumed that molecular adsorption of CO on the CuO_2-terminated surface is highly unlikely. This relative instability of the adsorption process in the CuO_2-terminated surface when compared with the

Cu-terminated surface can be attributed to the saturated surface Cu atoms due to the presence of surface O atoms.

Table 2.6: Adsorption energies (in eV) for CO on different adsorption sites on CuO (110). The values in parentheses indicate the obtained adsorption energies without van der Waals corrections.

Adsorption site	Geometry	Cu-terminated		CuO_2-terminated	
T_{Cu}-site	C-end	-0.84	(-0.47)	-0.15	(0.11)
	O-end	0.35	(0.51)	0.60	(0.86)
T_O-site	C-end	-		0.03	(0.28)
	O-end	-		0.65	(0.91)
B-site	C-end	-0.59	(-0.26)	-0.05	(0.14)
	O-end	0.32	(0.49)	0.35	(0.52)
H-site	C-end	-0.64	(-0.43)	0.22	(0.46)
	O-end	0.39	(0.55)	0.85	(1.15)

To connect the study with the obtained result for NO dissociation, the investigation proceeds with the molecular adsorption of CO on a Cu-terminated CuO(110) surface with an O adatom on a hollow site, hereby denoted as O_{ad}/Cu-terminated CuO(110) surface. It is assumed that the O adatom is a result of NO dissociation. The adsorption sites for CO adsorption are shown in Fig. 2.17. Because it has been established that the C-end configuration is the most stable, the adsorption energy for this geometry alone is calculated. The results are shown in Table 2.7, together with comparison with the Cu-terminated surface without the O adatom. It is important to note that the reference energy for calculating the adsorption energy is different for the Oad/Cu-terminated surface. For the E_{iso} term in Eq. 1, which is the summed energy of the isolated CO molecule and bare surface, the bare surface now includes the O adatom.

Similar with the Cu-terminated case without O adatom, the molecular adsorption of CO is most stable on the Cu top site of the O_{ad}/Cu-terminated CuO(110) surface as shown in Fig. 2.18a. The adsorption energy is -1.71 eV, compared with -0.84 eV for the case without O adatom. The distance between the C atom and the surface Cu atom is 1.98 Å, and the C-O bond length is 1.158 Å. The distance between the C atom and the O adatom is 2.83 Å and the O-C-O angle with respect to the surface is 93.0°. The additional information is necessary for the succeeding investigation on CO oxidation.
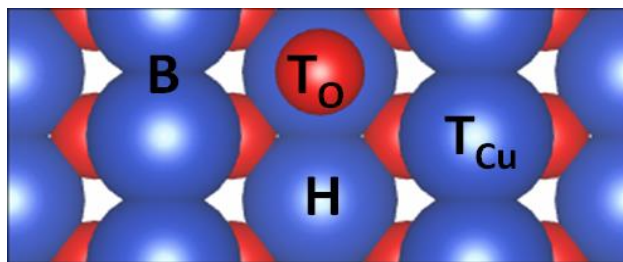
Figure 2.17: Top view of the O_{ad}/Cu-terminated CuO(110) surface. The high symmetry sites for CO adsorption are also indicated: T_{Cu} - Cu top site, T_O - O top site, B - bridge site, and H - hollow site.
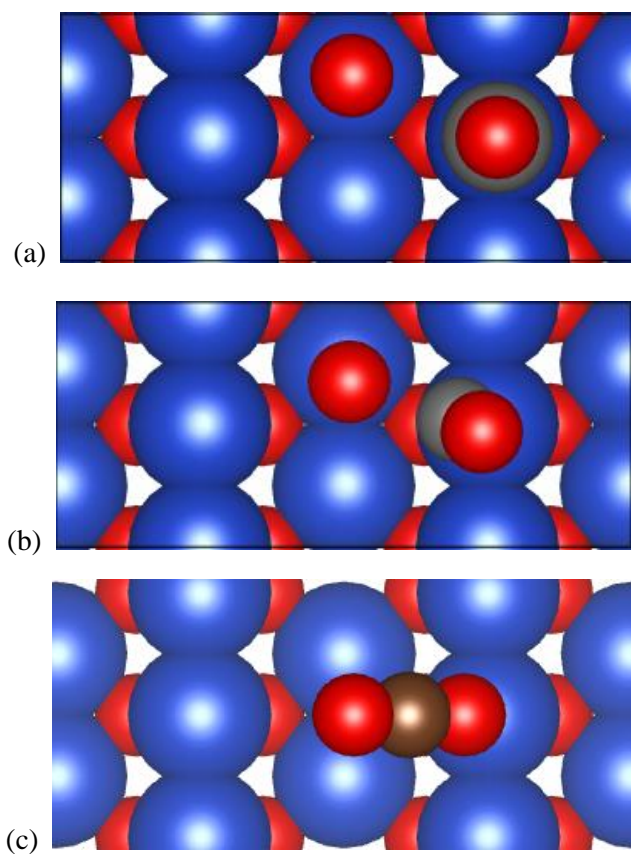
Figure 2.18: Stable structures (top view) of (a) the molecular adsorption of CO on Oad/Cu-terminated CuO(110), (b) transition state, and (c) molecular adsorption of CO_2 on Cu-terminated CuO(110) surface. The blue spheres represent Cu atoms, brown spheres represent C atoms, and red spheres represent O atoms.

Table 2.7: Adsorption energies (in eV) for CO on different adsorption sites on Cu-terminated CuO (110) with and without an O adatom. The values in parentheses indicate the obtained adsorption energies without van der Waals corrections.

Adsorption site	Cu-terminated		O_{ad}/Cu-terminated	
T_{Cu}-site	-0.84	(-0.47)	-1.71	(-1.46)
T_O-site	-		-0.98	(-0.70)
B-site	-0.59	(-0.26)	-1.57	(-1.32)
H-site	-0.64	(-0.43)	-1.52	(-1.34)

As the desired product of CO oxidation, the molecular adsorption of CO_2 on CuO(110) is likewise studied. CO_2 adsorption in general is an interesting topic in itself, which is due to its potential in the photocatalytic reduction of CO_2 into fuels such as methanol, which has become an attractive means of reducing CO_2 emissions as well as providing an alternative energy resource. CO_2 adsorption on Cu_2O has been previously studied [50-55]. Cu_2O has been successfully employed in the electrochemical reduction of CO_2 to methanol [50]. Further, the reduction of CO_2 on copper oxide with mixed oxidation states (Cu_2O, CuO, and Cu_4O_3), methanol yield qualitatively follows Cu(I) concentration [51]. Hybrid CuO-Cu_2O nanoarrays has also been used in the photoelectrosythesis of methanol from CO_2 [52]. However, theoretical studies have focused on CO_2 adsorption on Cu_2O [53-55]. While Cu_2O and the Cu(I) species has been widely studied, much is still to be understood about the interaction of CO_2 with CuO and the Cu(II) species.

Adsorption sites on both terminations of CuO(110) were investigated for CO_2 adsorption. Several geometries for the adsorbate were considered as the initial configurations prior to relaxation: with the molecule perpendicular to the surface, parallel to the surface, and tilted 45° with respect to the surface parallel. The adsorption energies are calculated using Eq. 1, where E_{ads} is the adsorption energy, E_{sys} is the calculated total energy of the system, and E_{iso} is the summed energy of the isolated CO_2 molecule and bare surface. The results are shown in Table 2.8. The most stable structure is when CO_2 is adsorbed with a tilted configuration on the Cu top site of the Cu-terminated surface, as shown in Fig. 2.18c, with an adsorption energy of -1.45 eV. The distance between the bottom O atom of the CO_2 molecule and the surface Cu atom is 2.04 Å, and the C-O distances within the CO_2 molecule remain unchanged compared to the equilibrium C-O bond length for gas phase CO_2 (calculated to be 1.165 Å in vacuum, which is in good agreement with the measured experimental value [56]). The optimized tilt angle is 32° with respect to the surface parallel. The CO_2 molecule mostly retains its linearity, with an

optimized O-C-O angle of 178°. For the other adsorption sites, the optimized geometries were either a configuration close to that of the Cu top site for the Cu-terminated surface, or a desorbed CO_2 molecule for the CuO_2-terminated surface.

Table 2.8: Adsorption energies (in eV) for CO_2 on different adsorption sites on CuO(110). The values in parentheses indicate the obtained adsorption energies without van der Waals corrections.

Adsorption site	Geometry	Cu-terminated		CuO_2-terminated	
T_{Cu}-site	perpendicular	-0.79	(-0.67)	0.77	(0.85)
	parallel	-1.35	(-1.21)	-0.02	(0.26)
	tilted	-1.45	(-1.25)	-0.11	(0.13)
T_O-site	perpendicular	-		0.93	(1.08)
	parallel	-		0.72	(0.81)
	tilted	-		0.26	(0.37)
B-site	perpendicular	-0.81	(-0.68)	0.82	(0.95)
	parallel	-1.22	(-1.08)	0.05	(0.21)
	tilted	-1.28	(-1.11)	-0.02	(0.15)
H-site	perpendicular	-0.76	(-0.65)	1.12	(1.26)
	parallel	-1.09	(-0.95)	0.35	(0.48)
	tilted	-1.15	(-0.93)	0.37	(0.53)

Denoting Fig 2.18a and 2.18c as the initial and final states respectively, the transition state was obtained using the CI-NEB method. The structure for the transition state is shown in Fig. 2.13b. The transition state has an adsorption energy of -0.90 eV, and the activation barrier to reach the transition state from the initial state is 0.81 eV. The distance between C and the O adatom has contracted to 2.10 Å, and the O-C-O angle with respect to the surface has changed from almost perpendicular to 109.7°. Vibrational frequency calculations showed the presence of imaginary frequencies, thus verifying the validity of the transition state. CO oxidation on CuO is exothermic, with the calculated transition state below the reference energy. This reaction path is comparable to the reported oxidation of CO on Rh(111) surface, both being exothermic [24].

2.6   Electric field effects

Electric fields, whether imposed or intrinsic, are capable of affecting the reaction of atoms and molecules on metal surfaces. They can have significant effects on the adsorption energies and reaction rates in heterogeneous catalytic systems. Thus, it is important to consider these effects in physical systems related to electrochemistry and catalysis [57]. Electric field effects on the adsorption of NO on Pt have been studied before in experiments and theoretical work. Although NO adsorbed on Pt does not dissociate at room temperature, applying steady electric fields can cause rapid decomposition [58]. Employing pulsed field desorption mass spectroscopy, N_2O^+, O^+, N_2^+ are observed as the field is increased. Decreasing amounts of NO were recorded, and at fields beyond 1.2 V/ Å, NO could no longer be observed at the Pt(111) surface. Computational studies using the semiempirical atom superposition and electron delocalization molecular orbital (ASED-MO) method agreed with the experimental results [59].

Recently, calculations on metal-adsorbate systems in an electric field have been performed using DFT with a slab model in a periodic supercell. In such a calculation, an external electric field can be implemented by introducing a dipole sheet in the middle of the vacuum region, thus polarizing the periodic slab and imposing a uniform electric field on either side of the slab [60]. Thus, the section aims to investigate the effects of electric fields on the adsorption of NO on CuO(110) through this method.

Table 2.9: Summary of data for the molecular adsorption of NO. E_{ads} is the adsorption energy, d_{N-O} is the N-O bond length, and e_N and e_O is the charge for the N and O atoms respectively as obtained from Bader Analysis.

Electric Field (V/Å)	E_{ads} (eV)	d_{N-O} (Å)	e_N	e_O
-0.05	-1.777	1.29	4.888	6.553
0	-1.780	1.30	4.890	6.555
+0.05	-1.784	1.31	4.894	6.560
+0.10	-1.793	1.32	4.900	6.566
+0.40	-2.131	1.38	4.918	6.582

A positive electric field indicates that it is in the direction emanating from the surface, while a negative field indicates that it is towards the surface. Without electric field, the adsorption energy obtained is 1.780 eV. The adsorbed NO molecule is 1.29 Å from the surface and the N-O

bond length is 1.30 Å. In comparison, with the presence of applied electric fields, the adsorption energy changes depending on the field direction. As the electric field is steadily increased up to +0.40 V/Å, the adsorption energy also increases. On the other hand, when a -0.05 V/Å electric field is applied, the adsorption energy decreases. The same effect is observed for the N-O bond length; an increase in electric field corresponds to an increased N-O bond length elongation. Bader analysis of the charge distribution revealed an increase in electron transfer from the Pt surface to adsorbed NO molecule as the applied electric field increases. Larger electric fields induce more accumulation of charge on the surface which enabled more electrons to be transferred to the adsorbate. The adsorption energies, N-O bond length and Bader charge data are summarized in Table 2.9.

2.7 Conclusions

Density functional theory-based calculations on the reduction of NO and oxidation of CO on copper oxide surfaces have been conducted. Strong molecular adsorption of NO was observed on the hollow sites of both $CuO(110)$ and $Cu_2O(111)$ and have shown better reactivity than $Cu(111)$. The Cu-terminated surfaces are preferred since the unsaturated surface Cu atoms relax with reference to the O atoms in the subsurface, thus forming active sites for NO dissociation. This is due to the modified electronic structure of the surface Cu atoms in the copper oxides wherein a shift of the d states towards the Fermi energy was observed as a result of the interaction with O atoms in the subsurface. Destabilization of the NO sigma bonds on the copper oxide surfaces promoted the easier dissociation of NO as the O atom separated and adsorbed on the adjacent hollow site. Furthermore, the excellent hybridization between the adsorbed NO molecule and the surface Cu led to the stability of the transition states for the case of the copper oxides, and the overall reaction was found to be exothermic. On the other hand, CO molecule adsorbed preferably on top of a surface Cu atom in the Cu-terminated surfaces. The adsorbed CO reacts with a coadsorbed O adatom, and not with a lattice O in an O-rich termination. Molecularly adsorbed CO_2 is formed, while the overall reaction was found to be exothermic in copper oxides. Based on these results, it can be said that copper oxides are good catalysts for NO reduction and CO oxidation.

Chapter 3

Oxygen Reduction in Hydrogen Fuel Cells: Carbon Nanotubes

3.1   Introduction

Since the discovery of carbon nanotubes (CNTs) by Iijima in 1991 [61], research in the field of CNTs has attracted a great deal of interest. They have fascinating properties that make them potentially useful in nanoscale electronic, spintronic, biomedical applications [62], and in fuel cell technology [3] as catalyst support and hydrogen storage [63-64]. Moreover, the possible end to fossil fuels has sparked the search for alternative sources of energy, leading to increased attention for hydrogen fuel cell research. One of these fuel cells is the proton exchange membrane fuel cell (PEMFC), which transforms the chemical energy liberated during the electrochemical reaction of hydrogen and oxygen to electrical energy as shown previously in Fig. 1.3.

The world today faces several challenges for its future energy needs. These include increasing global population, demands for higher standards of living, need for less pollution, need to avert global warming, and the possible end to fuel cells. This has triggered the search for clean and renewable alternative sources of energy. In the present world, internal combustion engines and turbines are still widely used. These run on hydrocarbon fuels where the carbon is released to the atmosphere, does making it a major pollutant. Fuel cells can replace these as the primary way to convert chemical energy into kinetic or electrical energy.   However, fuel cells are more expensive to produce than common internal combustion engines. For PEMFC's, this is mainly because of the lack of an alternative to platinum as catalyst. But with continued research on alternative catalyst materials, these hydrogen fuel cells could be made available commercially in the near future.

In this study, the interaction of oxygen with SWCNTs through looking at the possible effects of the nanotube size, in particular its surface curvature, and filling with Fe-nanowire, was investigated. First principles calculations were employed to investigate the adsorption energies and stable structures for oxygen adsorption on SWCNTs with varying diameters and electrical properties, as well as graphene. Furthermore, insights on the effect of surface curvature and Fe-filling were pursued by looking at the differences in the charge distributions. The results we obtained will be useful in designing potential catalysts for oxygen reduction in the PEMFC.

3.2 Why carbon based catalysts?

Carbon-based nanomaterials such as fullerenes, graphene, and carbon nanotubes (CNTs) have attracted much attention for their fascinating properties that open possibilities for many applications. Platinum-decorated single-walled carbon nanotubes (SWCNTs) are presently being evaluated as catalyst material for oxygen reduction in PEMFC cathodes [63]. CNTs filled with ferromagnets demonstrate very high potential in providing modified magnetic properties, low dimensionality, and small volume which make them possible for many applications [65-71]. In particular, the magnetic and electronic properties of Fe-filled SWNTs were found to differ with varying nanotube diameters [72]. In addition, the SWNTs encapsulating Fe nanowires were found to transform into an arch-like structure when the Fe nanowire is near a Ni(111) surface [73-74]. Moreover, the durability of the PEMFC has been recently recognized as one of the most important issues to be addressed before its commercialization [75-79]. Pt surface area loss due to carbon support corrosion and Pt dissolution/ aggregation is considered one of the major contributors of failure for the PEMFC [76]. Carbon black (Vulcan XC-72), which is the normally used catalyst support for the PEMFC, is known to undergo chemical oxidation to surface oxides, and eventually to carbon dioxide at the cathode of a fuel cell. [80] It was found by a previous study that Pt accelerated the corrosion rate of carbon black. [81] There is a need to use alternative more stable carbon support. It has been proposed that carbon material with more graphite component (eg. carbon nanotubes) can be more stable.

The interaction of SWCNTs with oxygen has been widely studied for fundamental and practical purposes. Exposure of SWCNTs to oxygen has been found to dramatically influence its electrical resistance, thermoelectric power, and local density of states (LDOS) [82]. Experiments have shown that oxygen adsorption can induce a significant increase in the emission current of CNT field emitters [83]. Also, oxygen adsorption induces p-type doping in CNT-based field effect transistors [84]. Moreover, the purification of synthesized CNTs could

also be done through oxidation at elevated temperatures where the ambient oxygen reacts with the strained C-C bonds [85-86]. All of these previous studies suggest that oxygen is highly reactive with CNTs. However, the group of Barberio [87] found that there is no indication of oxygen adsorption for pristine and clean nanotubes. They exposed the SWCNTs to 1x10-6 Torr molecular oxygen at room temperature and found no evidence of interaction and mentioned that the strong sp^2 bonding of the graphitic ring structure may somehow prevent oxygen attachment to the SWCNT surface. Thus, a better understanding of the interaction between oxygen and CNTs is still needed.

3.3   Computational model

The atomic and electronic structures of the adsorbate-substrate systems are obtained using calculations based on density functional theory [32-33] and are performed using the Vienna ab initio simulation package (VASP) [34-35]. The theoretical background and implementation of this method are discussed in the Appendix. The electron-ion interaction is treated using the Projector Augmented Wave (PAW) method [36]. The Kohn-Sham (KS) one-electron valence states are solved in a periodic system by expanding the wave function in a basis of plane waves with an energy cutoff of 550 eV. The exchange-correlation energy is based on the generalized gradient approximation (GGA) using the Perdew-Burke-Ernzerhof (PBE) functional [37-38]. To account for possible effects of long-range dispersion or van der Waals interactions, the DFT-D2 method of Grimme [39] is used to introduce empirical corrections for dispersion interactions to the DFT calculations. The k-point sampling of the one dimensional Brillioun zone for the SWCNTs was obtained using 35 Monkhorst-Pack k-points [44] along the nanotube axis, while a 9 x 9 x 1 grid was obtained for graphene. All calculations were spin polarized and were done until the energy of the systems converge to 0.01 eV/A. In this study, the atomic and molecular adsorptions of oxygen were both investigated. Four different chiralities of SWCNTs were considered: (3,3), (5,0), (5,5) and (8,0) SWCNTs to provide not only an equal representation of armchair and zigzag SWCNTs but also have two pairs of nanotubes with the roughly the same diameters but different electronic properties. A vacuum distance of roughly 20 Å between neighboring SWCNTs was used to eliminate the effect of periodicity within the intertube distances. An initial magnetic moment of 2.0 μB was used for the oxygen atoms.
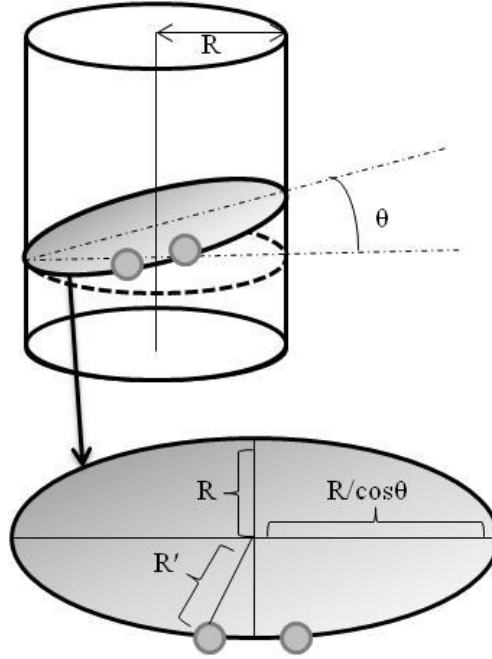
Figure 3.1: Schematic representation of the cross-section of a nanotube with radius R to show the local curvature radius, R′, along the C-C bond inclined by angle θ.

To analyze the effect of surface curvature, the local curvature radius, R′, of the SWCNTs was considered based on the C-C bond involved in the adsorption process. For the case of armchair SWCNTs, the C-C bond is along the circumferential axis, i.e. perpendicular to the tube axis, and thus, R′ is simply equal to the tube radius. This is because the cross section of the tube along the C-C bond is round. On the other hand, for the case of zigzag SWCNTs, R′ is larger than the tube radius since the cross section along the C-C bonds is ellipsoidal. We calculated R′ along the C-C bond using the equation [88]:

$$R' = \frac{R}{\cos^2(\pi/6 - \theta)},$$

where R is the radius of the SWCNT and theta (θ) is the chiral angle, as shown in Fig. 3.1.

The adsorption of atomic oxygen was investigated by placing the oxygen adatom on the bridge site between the C-C bonds, as shown in the unit cells for the SWCNTs in Fig. 3.2. On the other hand, the molecular adsorption of oxygen was examined by placing the oxygen molecule on the same bridge sites as in Fig. 3.2. Two orientations of the O_2 molecule were analyzed as shown in Fig. 3.3: parallel and perpendicular to the C-C bond axis. A potential energy scan (PES) was conducted for varying values of the O-O bond length, r, and the distance of the O_2 molecule

36

from the surface, z. The configuration with the minimum energy was fully-relaxed in order to obtain the adsorption energy and optimized geometry.

Figure 3.2: The unit cells of (a) (3,3) SWCNT, (b) (5,0) SWCNT, (c) (5,5) SWCNT, and (d) (8,0) SWCNT. Grey spheres indicate carbon atoms while the yellow circles show the bridge adsorption sites.

The adsorption energy of the system, E_{ads}, is the same as defined in Eq. 1, where E_{sys} is the total energy of the system and E_{iso} is the sum of the energies of the isolated SWCNT and oxygen atom or molecule. The summary of the properties of the SWCNTs used in this study are summarized in Table 3.1.

(a)   (b)
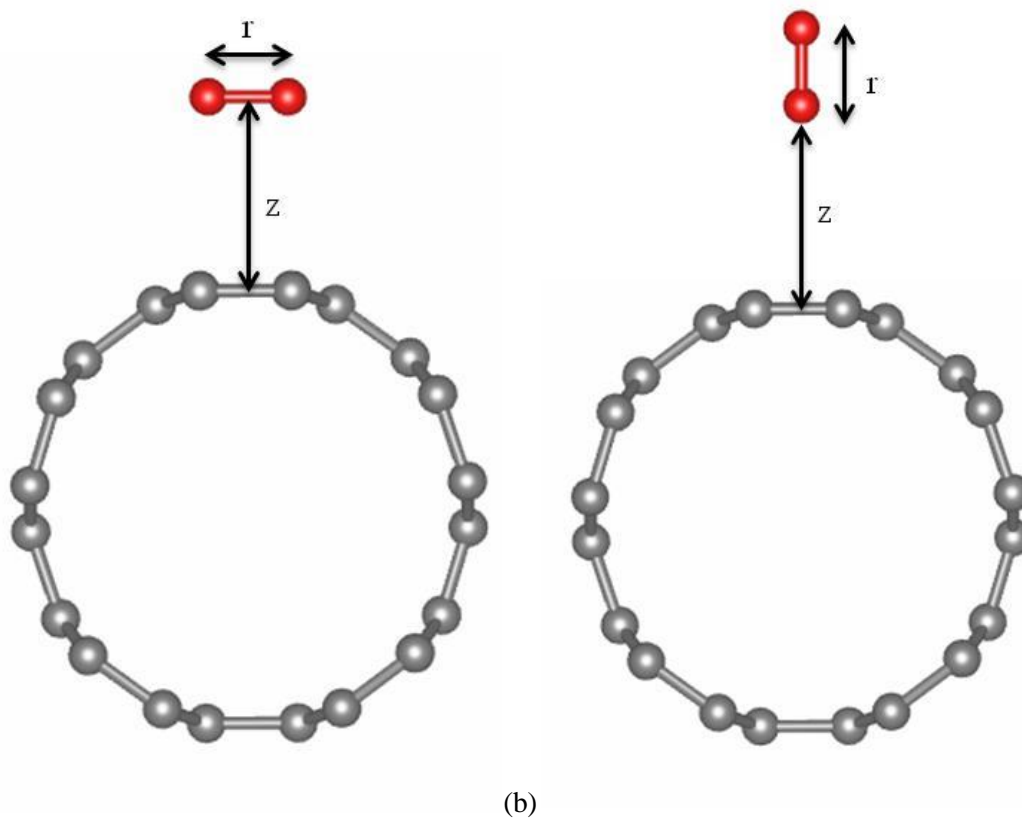
Figure 3.3: Schematic representation of the potential energy scan (PES) analysis for the molecular adsorption of oxygen on a (5,5) SWCNT for the oxygen molecule (a) parallel and (b) perpendicular to the C-C bond on the bridge site. The bond length, r, and the distance of the molecule from the bridge site, z, were varied. Grey spheres represent carbon atoms while red spheres represent oxygen atoms.

Table 3.1: Properties of SWCNT chiralities used in this study.

Chirality	Unit cell size	Tube diameter (in Å)	Curvature radius (in Å)	Electronic Property	
				Pristine	Fe nanowire-filled
(3,3)	24	4.07	2.04	Metallic	Semi-conducting
(5,0)	20	3.92	2.32	Semi-conducting	Semi-conducting
(5,5)	40	6.78	3.39	Metallic	Metallic
(8,0)	32	6.27	3.71	Semi-conducting	-

3.4   Adsorption of Oxygen on Pristine SWCNT

The adsorption of atomic oxygen on the bridge site was investigated to find out the effect of local surface curvature on the stability of an oxygen adatom on the SWCNT surface. The stable structures for O atom on the SWCNTs are shown in Fig. 3.4 and the adsorption energies, O magnetization and some structural parameters are tabulated in Table 3.2. The results instantly reveal a straightforward relationship between the surface curvature and the adsorption energy; as the curvature increases (i.e. decreasing R′), the adsorption energy increases as well. The large energies indicate strong chemisorption of the O atom with a significant charge transfer from C to O, and that the charge transfer is enhanced by greater curvature.

(a)   (b)

(c)   (d)

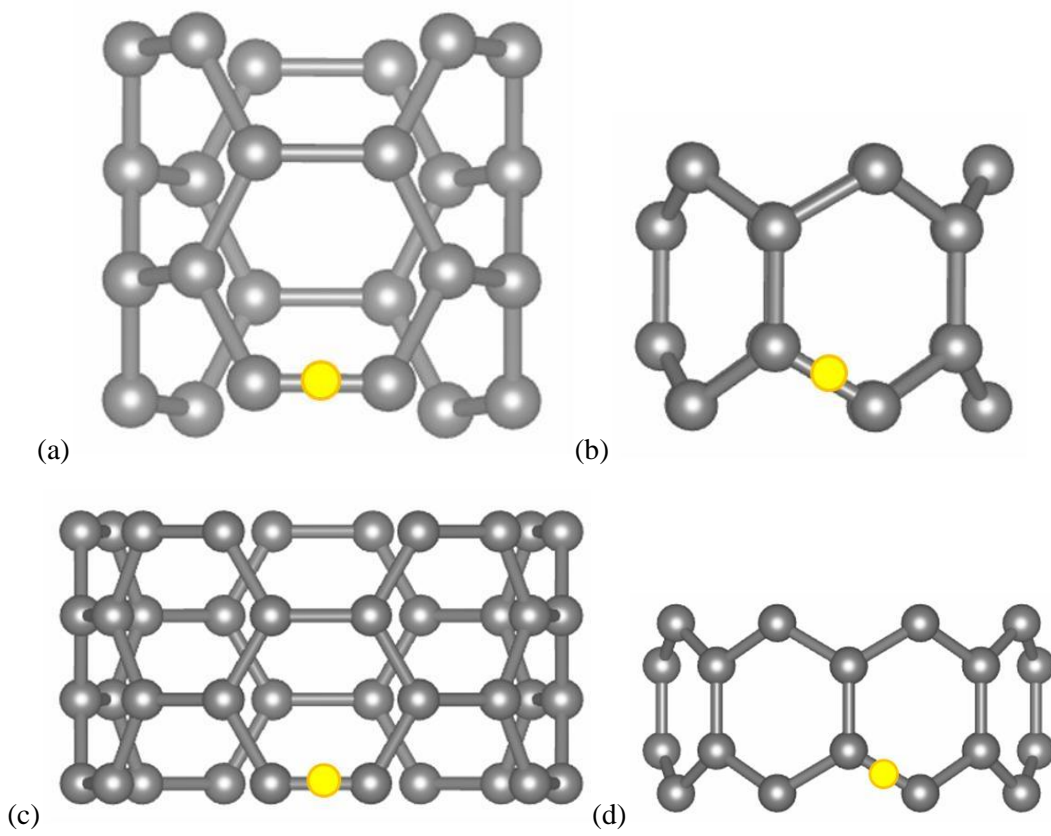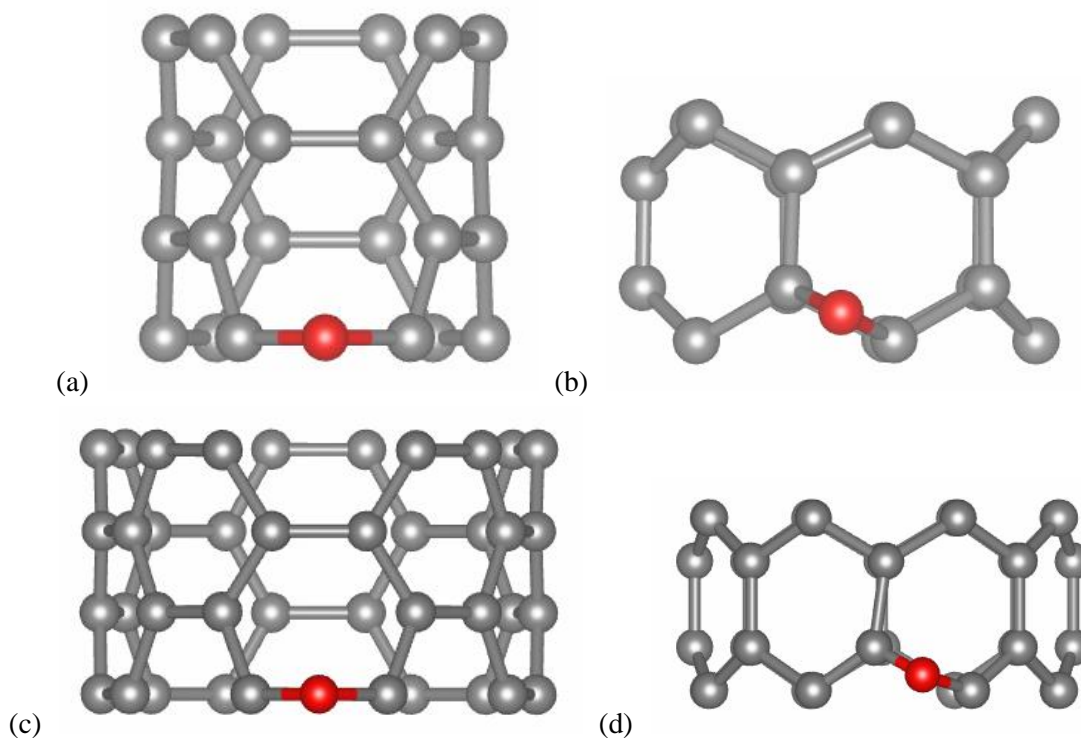**Figure 3.4:** Optimized structures for the adsorption of oxygen on the bridge sites of (a) (3,3) SWCNT, (b) (5,0) SWCNT, (c) (5,5) SWCNT, and (d) (8,0) SWCNT. Grey spheres represent carbon atoms while red spheres represent oxygen atoms.

Table 3.2: Adsorption energy (E_A), magnetization, and geometric configuration data for oxygen atom adsorption. C_1 and C_2 indicate the two carbon atoms in the bridge site.

SWCNT	Diameter (Å)	R′ (Å)	E_A (eV)	Magnetization of O (μ_B)	Interatomic distances (Å) O-C_1	O-C_2	C_1-C_2
(3,3)	4.07	2.04	-6.91	0	1.41	1.41	2.14
(5,0)	3.92	2.32	-5.70	0	1.43	1.43	1.50
(5,5)	6.78	3.39	-5.52	0	1.40	1.40	2.17
(8,0)	6.27	3.71	-5.07	0	1.39	1.39	2.18

To confirm this, the charge distribution was analyzed by looking at the contour plots of the charge density on planes passing through the chemisorbed O atoms on the bridge sites, as shown in Fig. 3.5. It can be seen that the C-C bond is destroyed and that new C-O bonds have formed for the (3,3) SWCNT. This was not the case for the (5,0) SWCNT, as the C-C bond was still intact. Furthermore, there is a greater overlapping of charges between the oxygen and carbon atoms in the (3,3) SWCNT as compared with the (5,0) SWCNT. Though both have quite similar diameters, the one with the lower R′ has more charge transfer. This is clearly seen from the Bader analysis of the charge distribution in Table 3.3.

(a)   (b)
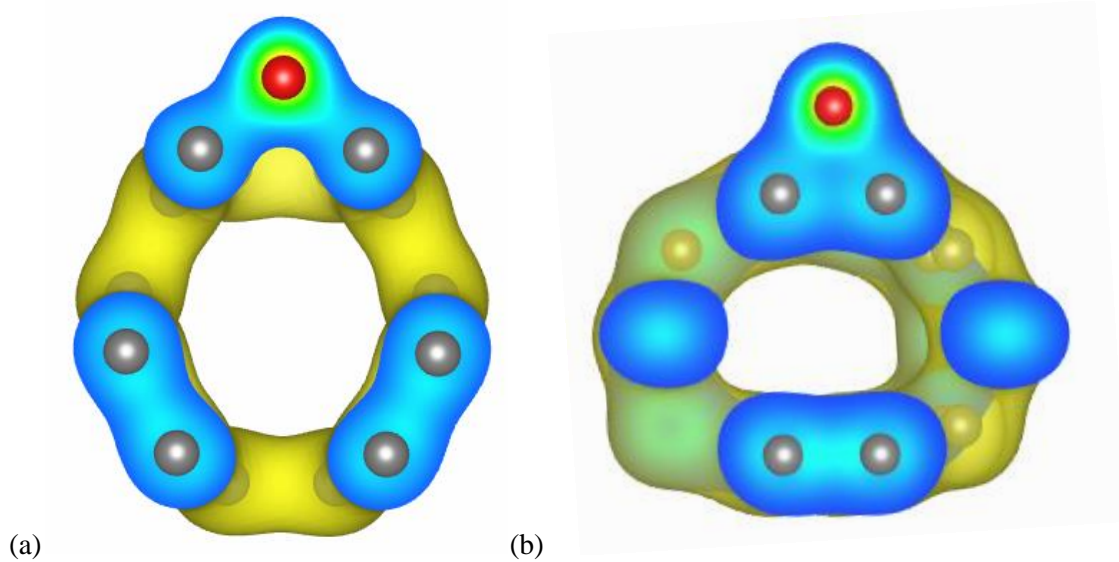
Figure 3.5: Charge density distribution for (a) (3,3) SWCNT and (b) (5,0) SWCNT. Grey spheres represent carbon atoms while red spheres represent oxygen atoms, with an isosurface level of $0.11a_0^{-3}$ (a_0: Bohr radius)

The energy of the anti-bonding π^* states increased for all cases, implying a depletion of anti-bonding states near the Fermi energy, which is consistent with the stable adsorption energies obtained. In effect, for the semiconducting cases, the HOMO-LUMO gap increased by about 3% after oxygen adsorption. Lastly, the singlet state with a net zero magnetic moment was found to be the ground state from the spin-polarized optimization, which explains the disappearance of the magnetization of the oxygen atom upon adsorption.

It is interesting to note that the C-C bond was not destroyed only for the case of (5,0) SWCNT. One reason for this could be due to the very small size of the SWCNT unit cell. The flattening of the nanotube can be seen in (5,0) case as the structure bulges out on the sides of the bridge site where the O atom is adsorbed. Thus we can see more interaction between the carbon atoms that limits the capacity of the receiving C atoms on the bridge site to interact with the oxygen. This also explains the lower charge transfer on the (5,0) case. These observations are consistent with previous studies, both theoretically [88] and experimentally [89-90], wherein the (5,0) SWCNT was found to be significantly more robust than the (3,3) and (4,2) SWCNTs, all three of which have similar diameters. So with the exception of the (5,0) SWCNT, a trend can be generalized that relates the charge transfer with the R'. As the curvature decreases, we see both a decrease in adsorption energy and charge transfer. In the case of the flat graphene surface, we obtained an adsorption energy of -4.51 eV, which is comparable with the value obtained by the group of Ishii [91], and a charge transfer of 0.43 electrons from the surface to the oxygen atom. Thus the trend holds that the values we obtained for the adsorption energy and charge transfer approached that of the values for graphene as curvature decreases.

Table 3.3: Charge difference for the adsorption of O atom on the bridge site of SWCNTs. The values shown are in units of e as obtained from the analysis of the Bader Charge. Positive and negative values refer to the accumulation and depletion of charges respectively. C_1 and C_2 indicate the two carbon atoms in the bridge site.

Atom	Charge Difference			
	(3,3) SWCNT	(5,0) SWCNT	(5,5) SWCNT	(8,0) SWCNT
O	0.621	0.260	0.485	0.462
C_1	-0.289	-0.124	-0.238	-0.214
C_2	-0.295	-0.128	-0.239	-0.211

For the molecular adsorption of oxygen on the SWCNTs, a potential energy scan (PES) for different values of the oxygen molecule bond length, r and the distance of the oxygen molecule

from the bridge site, z, for two configurations of the oxygen molecule was performed as shown in Fig. 3.3. At first, static calculations were done to find the values for r and z that correspond to the minimum energy. Using the minimum energy configuration from the PES, the system was optimized to obtain the final adsorption energies and structural parameters for the molecular adsorption of oxygen on SWCNTs. The minimum energy was found at a distance between 3.0 Å and 3.5 Å for all cases. The adsorption energies and structural parameters from the optimized calculations are shown in Table 3.4. From the results, weak binding of the oxygen molecule with the SWCNTs are seen, with adsorption energies below -0.5 eV and are characteristic of physisorption. Most of the interaction between the oxygen molecule and the SWCNTs arise from the long-range van der Waals interactions. The adsorption energies obtained from calculations without the van der Waals correction were in the range of 15-25 meV, consistent with previous DFT studies [92-93]. Again, a trend of increasing adsorption energy for greater curvature is observed. Bader analysis of the charge distribution showed minimal charge transfer between the surface and the oxygen molecule and with distances of more than 3 Å apart, it is unlikely that the orbitals interact efficiently with each other. Furthermore, no changes were observed to the magnetization of the oxygen atoms.

Table 3.4: Adsorption energy (E_A) and geometric configuration data for oxygen molecule adsorption from DFT-D2 caclulations. O_1 and O_2 indicate the two oxygen atoms in the oxygen molecule.

SWCNT	Diameter (Å)	R′ (Å)	E_A (eV)	Magnetization (μ_B)		Distances (Å)	
				O_1	O_2	r	z
(3,3)	4.07	2.04	-0.32	2	2	1.23	3.19
(5,0)	3.92	2.32	-0.27	2	2	1.23	3.32
(5,5)	6.78	3.39	-0.14	2	2	1.23	3.48
(8,0)	6.27	3.71	-0.13	2	2	1.23	3.37

Planar sp^2 bonding characteristic of graphene plays a significant role in SWCNTs since basically, SWCNTs are just graphene sheets rolled up into cylinders. However, due to the surface curvature in SWCNTs, the carbon atoms acquire sp^3-like properties that weaken the binding of the carbon atoms along the circumferential axis as compared with the nanotube axis. C-C bonds along the nanotube axis are considered to have an infinite R′ and are thus flat. Due to this weakening of the bonding between carbon atoms, curvature plays an important effect in the ability of the SWCNTs to interact with adsorbates as compared with the flat graphene sheet. In our case, greater curvature allowed the C-C bonds along the circumferential axis to weaken and

thus allowed better interaction with oxygen. This is particularly evident in the adsorption of atomic oxygen and to a lesser extent, also to the adsorption of the oxygen molecule. The only exception is the (5,0) SWCNT, due to its robust structure. Thus, if we can design carbon materials in such a way that we can induce sp^3-like properties, i.e. introducing sp^3-inducing defects on graphene and SWCNTs, we can greatly enhance its activity with oxygen and make them useful in many applications, such as for oxygen reduction in the PEMFC.

3.5   Adsorption of Oxygen on Fe-filled SWCNT

The adsorption of atomic oxygen on the bridge site of Fe-filled SWCNT was investigated to find out the effect of the presence of Fe nanowire inside the SWCNT on the stability of an oxygen adatom on the SWCNT surface.
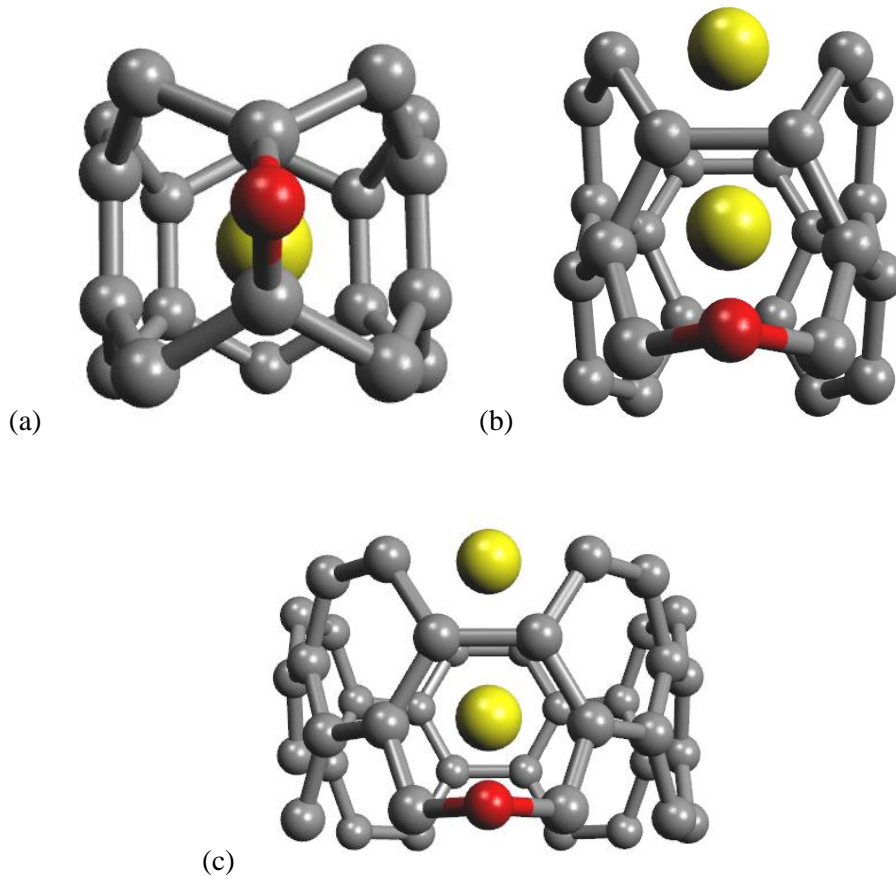

(a)   (b)

(c)

Figure 3.6: Stable structures for oxygen atom adsorption for (a) (5,0) (b) (3,3), and (c) (5,5) Fe-filled SWCNT.

The stable structures for O atom on the Fe-fileld SWCNTs are shown in Fig. 3.6 and the adsorption energies, O magnetization and some structural parameters are tabulated in Table 3.5. The adsorption energies are weaker for the Fe-filled cases when compared with the pristine cases. Furthermore, the adsorption energies tend to decrease with decreasing curvature radius, similar to that of pristine SWCNT. The magnetic moments of the O and Fe atoms disappeared for the Fe-filled cases.

Table 3.5: Adsorption energy (E_A), magnetization, and geometric configuration data for oxygen atom adsorption. C_1 and C_2 indicate the two carbon atoms in the bridge site.

System	E_A (eV)	Magnetization (μ_B)		Interatomic distances (Å)		
		O	Fe	O-C_1	O-C_2	C_1-C_2
(3,3) Pristine	-6.91	1	-	1.41	1.41	2.14
(3,3) Fe- SWCNT	-5.57	0	0	1.43	1.43	2.10
(5,0) Pristine	-5.70	1	-	1.43	1.43	1.50
(5,0) Fe-SWCNT	-4.50	0	0	1.42	1.42	1.55
(5,5) Pristine	-5.52	1	-	1.40	1.40	2.07
(5,5) Fe- SWCNT	-3.93	0	0	1.40	1.40	2.08

The PES calculations for the oxygen molecule was performed by calculating the adsorption energies for different values of the oxygen molecule bond length, r and the distance of the oxygen molecule from the adsorption site, z. Since the bridge site was found to be the most stable site for atomic adsorption, the reaction path considered for molecular adsorption has the oxygen molecule approach the SWCNT in such a way where both oxygen atoms would adsorb on opposite bridge sites. The resulting potential energy surfaces (PES) were analyzed. Fig. 3.7 shows the PES for the case of (3,3) Fe-SWCNT. The oxygen molecule approaches the SWCNT surface, it encounters an energy barrier of about 1.3 eV before it can dissociate. The minimum energy before the barrier, which we shall call the molecularly adsorbed state, was found to be -0.21 eV at a height of 2 Å from the SWCNT surface. After the barrier we have a second minimum energy at -0.53 eV and the oxygen atoms are 1.2 Å from the SWCNT surface and are separated by 2.48 Å. We shall call this the dissociated state. With the molecularly adsorbed and dissociated states from the PES calculations, we employ the CI-NEB method to obtain the transition state (TS) and corresponding energy barrier. The TS energy for the (3,3) Fe-SWCNT was 1.14 eV, corresponding to an energy barrier of 1.35 eV, which is comparable to the obtained value from the PES. The results of the other cases, summarized in Table 3.6, reveal a consistent

trend – that the oxygen molecule is stable with low adsorption energy that is characteristic of molecular physisorption and that a significant energy barrier must be overcome for dissociation to occur.
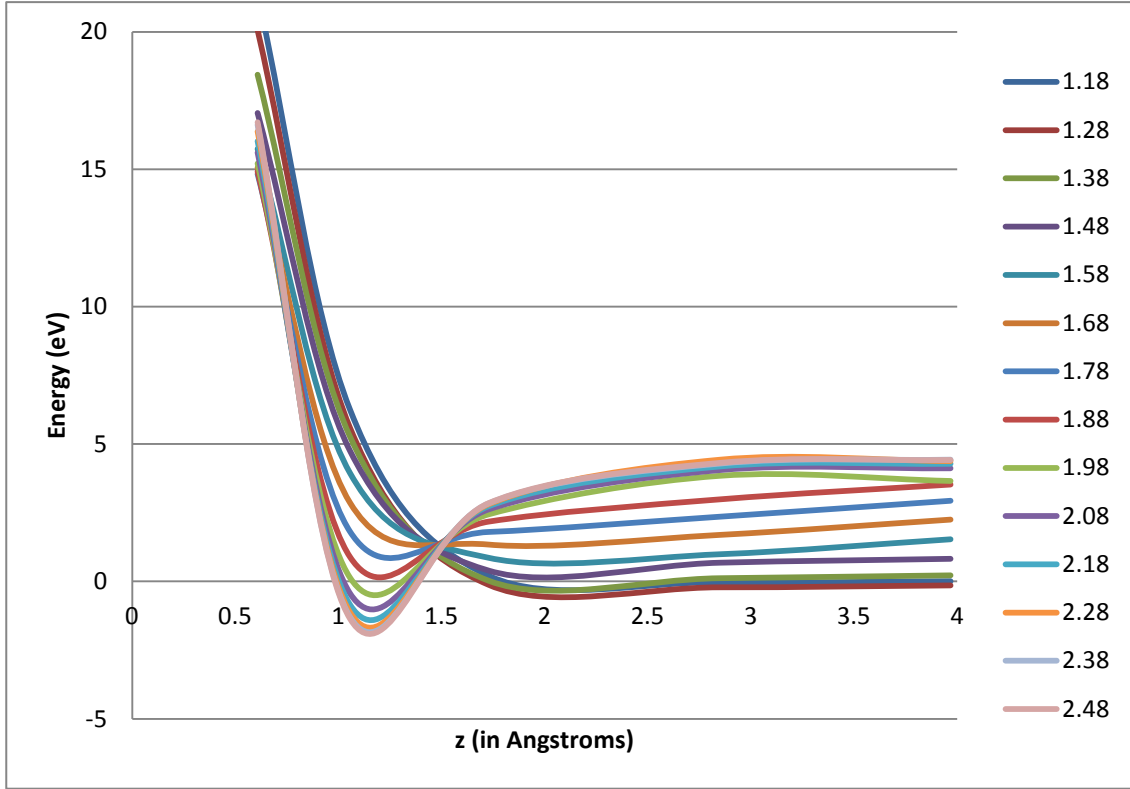
Figure 3.7: Potential energy surface (PES) for oxygen molecule adsorption on (3,3) Fe-SWCNT.

Table 3.6: PES analysis and cNEB data for oxygen molecule adsorption where E_i and E_f are the adsorption energies of the initial and final states from the PES, E_B is the energy barrier also from the PES, and E_{TS} is the energy barrier of the transition state from the CI-NEB.

System	E_i (eV)	E_f (eV)	E_B (eV)	E_{TS} (eV)
(3,3) Pristine	-0.32	-1.35	1.96	1.64
(3,3) Fe- SWCNT	-0.21	-0.53	1.35	1.14
(5,0) Pristine	-0.27	2.12	5.16	4.89
(5,0) Fe-SWCNT	-0.19	1.26	3.29	3.32
(5,5) Pristine	-0.14	0.27	0.45	0.55
(5,5) Fe- SWCNT	-0.10	0.18	0.37	0.42

However, the energy of the dissociated state for the (5,0) and (5,5) cases are above the reference energy. Thus we conclude that dissociation is not favored for these cases. Moreover, when comparing the reactivity of oxygen on Fe-SWCNT with the pristine cases, the general trend is that the molecular physisorption energies are stronger whereas the adsorption energy of the dissociated cases and its corresponding energy barriers are lower for Fe-SWCNT cases. This can be attributed to the modified electronic structure of the nanotube due to the effect of Fe. The surface carbon atoms in the vicinity of Fe have a depletion of occupied states near the Fermi level as compared to the surface C atoms of the pristine SWCNT. This explains the weaker adsorption of dissociated states on Fe-SWCNT. However, there is a slight enhancement of the charge transfer from the surface carbons atoms of Fe-SWCNT to the molecularly adsorbed oxygen, thus explaining the stronger molecular physisorption. This combination makes Fe-SWCNT better than pristine SWCNT for oxygen reduction as it promotes stronger molecular adsorption, as well as easier desorption of the dissociated atoms.

3.5   Hydrogen Peroxide Poisoning

Hydrogen peroxide has been found to oxidize semiconducting SWCNT by the active oxygen produced during its decomposition [94]. It oxidizes the semiconducting SWCNT more favorably than metallic ones. The degradation kinetics of SWCNT in H_2O_2 was strongly dependent on the amount of metal particle catalysts remaining in the sample. This clearly shows that the presence of Fe nanoparticles within the samples promoted the oxidation of SWCNT in H_2O_2. It is likely that the decomposition of hydrogen peroxide was catalyzed by Fe nanoparticles, and the active oxygen was responsible for attacking the SWNT. H_2O_2-induced oxidation of SWCNT is good from two perspectives: the low-temperature combustion of SWCNT without the formation of byproducts and the enhanced chemical reactivity of SWCNT afforded by hole-doping, as shown in Fig. 3.8.

Fe is also known to catalyze the decomposition of hydrogen peroxide [95]. Moreover, some studies found that the Nafion® membrane and membrane electrode assembly (MEA) of PEMFC's become very unstable in the presence of hydrogen peroxide, which is formed as a by-product [96-98], due to its strong oxidative properties [99-103]. There are two different mechanisms for H_2O_2 generation in the PEMFC. The first is O_2 reduction at the cathode during operation, described earlier as

$$O_2 + 2H^+ + 2e^- \rightarrow H_2O_2$$
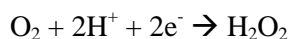
The other pathway is based on O_2 cross-over from the cathode, through the membrane, to the anode side, which provides the O_2 needed to react with hydrogen to produce H_2O_2. [100-101], i.e.:

$$2Pt + H_2 \rightarrow 2PtH$$
$$2PtH + O_2 \rightarrow Pt + H_2O_2$$
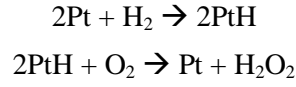
Hydrogen peroxide in itself does not attack the polymer electolyte membrane. Rather, it reacts with trace metal ions to form $HO\cdot$ and $HOO\cdot$ radicals that attack the membrane [102-103]. The process for producing hydroxyl radicals is known as the Fenton reaction [104-108], i.e.:

$$Fe^{2+} + H_2O_2 \rightarrow Fe^{3+} + HO\cdot + OH-$$
$$H_2O_2 + HO\cdot \rightarrow H_2O + HOO\cdot$$
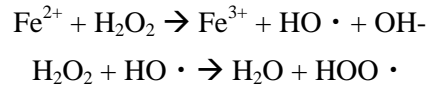
Thus, research on the reduction of hydrogen peroxide generation must be investigated to prevent degradation of the membrane and to obtain long-term PEMFC stability. [109]
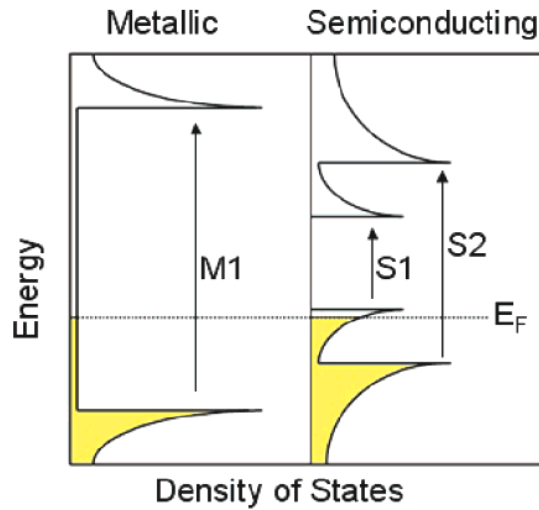
Figure 3.8: Proposed hole-doping effect of hydrogen peroxide on SWCNT as shown by the density of states of metallic and semiconducting SWCNT. [94]

Therefore, if hydrogen peroxide is reacted with Fe-filled SWCNT, it is expected that the hydrogen peroxide would either oxidize and destroy the SWCNT or dissociate into water and

oxygen and other derivatives such as hydroxyl radicals or hydrogen itself.

The adsorption energies from the PES calculations were likewise obtained using Eq. 1, where E_{sys} is the total energy of the system in the fixed calculation and E_{iso} is the sum of the energies of the isolated SWCNT (pristine or Fe-filled) and H_2O_2 molecule. The results from the PES calculations are shown in Table 3.7. The minimum energies obtained indicate weak interaction between H_2O_2 and the SWNT. The equilibrium distance was found to be 3.75 Å for most cases. Optimization at the equilibrium distances indicated that the H_2O_2 was molecularly adsorbed on the SWNTs. Thus, the minimum energies are considered as the physisorption energy (E_P). The H_2O_2 molecule prefers to be adsorbed on the B-sites for the (3,3) cases while the H-site is preferred for the (5,5) cases, although the difference in adsorption energies among all adsorption sites are minimal. Due to this weak interaction, dissociation of the H_2O_2 molecule might be needed for a stronger interaction with the SWNT surface.

Table 3.7: Equilibrium distances and minimum energies obtained from PES calculations

Adsorption Site	(3,3) SWNT		(5,5) SWNT	
	Distance (Å)	Energy, E_P (eV)	Distance (Å)	Energy, E_P (eV)
Pristine B-site	4.00	-0.017	3.75	-0.014
Pristine T-site	3.75	-0.016	3.75	-0.014
Pristine H-site	3.75	-0.016	3.75	-0.016
Fe-filled B-site	3.75	-0.018	3.75	-0.015
Fe-filled T-site	3.75	-0.015	3.75	-0.015
Fe-filled H-site	3.75	-0.016	3.75	-0.018

After obtaining the stable position for molecular adsorption, dissociative chemisorption was investigated by finding the most preferable positions for H_2O_2 that has been dissociated into a hydroxyl pair. Fig. 3.9 shows the most stable structures. It can be noted that the hydroxyl pairs prefer to be adsorbed on opposite carbon top sites. This led to the elongation of the C-C bonds on the SWCNT surface, though in most cases bond-breaking did not occur. The only exception is the semiconducting (3,3)-Fe-filled case where bond-breaking of the C-C bonds on the

SWCNT surface was observed.
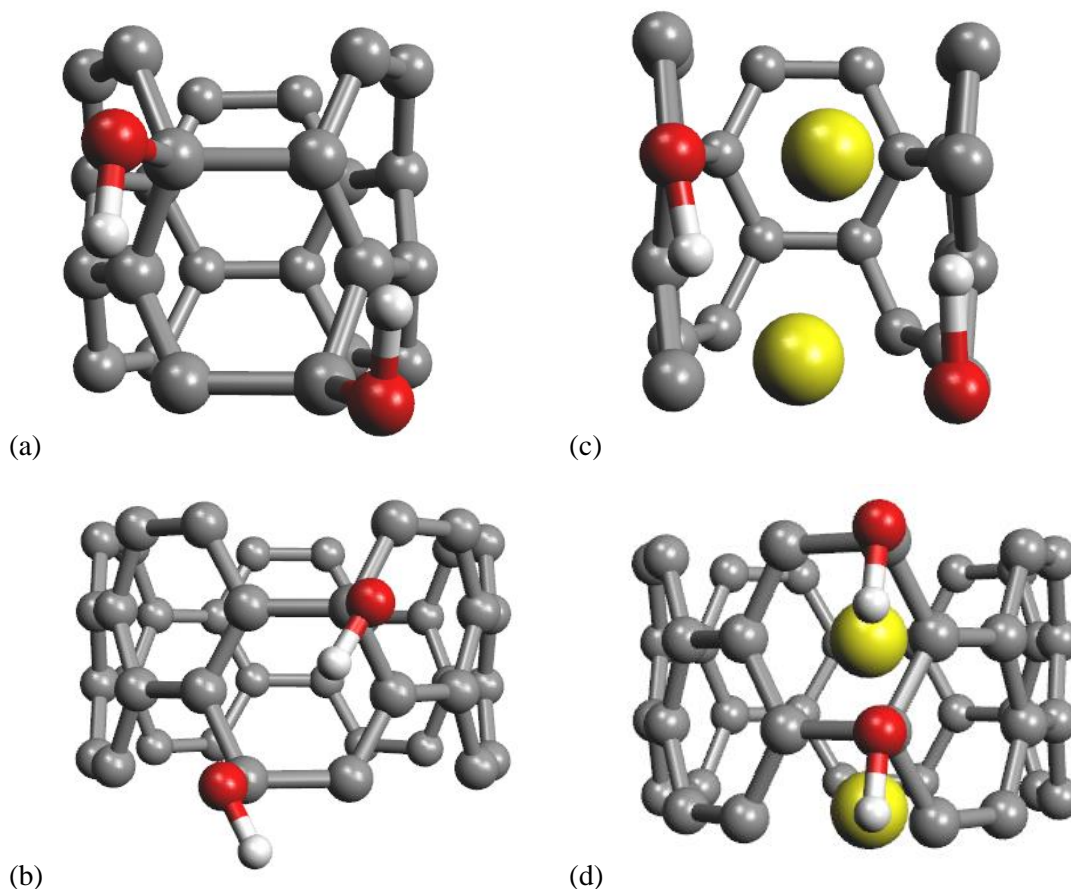
Figure 3.9: Stable structures for hydrogen peroxide adsorption for (a) (3,3) pristine SWNT, (b) (5,5) pristine SWNT, (c) (3,3) Fe-SWNT, and (d) (5,5) Fe-SWNT.

Using the resulting energies from the optimization, the chemisorption energies (E_C) were calculated and the results are shown in Table 3.8. For this case, E_{sys} is the total energy of the system after optimization and E_{iso} is the sum of the energies of the isolated SWNT (pristine or Fe-filled) and H_2O_2 molecule. The large values for the energies indicate stronger interaction of the hydroxyl radicals as compared with the H_2O_2 molecule. It can be noted that the Fe-filled cases have larger chemisorption energies than the pristine cases. Therefore, it is more likely for the Fe-filled cases to have a lower dissociation energy barrier as compared to pristine cases.

The existence of energy barriers was investigated through further examination of the reaction pathway from the physisorbed states to the dissociated chemisorbed states. PES calculations were done for different O-O bond lengths of the H_2O_2 molecule. Energy barriers (E_B) in the

49

order of 10^{-2} eV were obtained for all cases and the results are shown in Table 3.8. Because the values for the energy barriers are minimal, the pathways examined can be thought of as barrierless reactions.

Table 3.8: Adsorption and dissociation energies for dissociative chemisorption.

Case	Adsorption Energy, E_C (eV)	Dissociation Energy, E_B (eV)
(3,3) Pristine	-2.56	0.035
(3,3) Fe-filled	-7.76	0.029
(5,5) Pristine	-1.87	0.054
(5,5) Fe-filled	-3.36	0.046

3.7   Conclusions

We have analyzed the effect of surface curvature on the adsorption of atomic and molecular oxygen on SWCNTs and graphene through the investigation of its adsorption energetics, structural properties, and charge distributions using first principles calculations based on density functional theory (DFT). We found that the oxygen atom is strongly chemisorbed on the bridge site of the SWCNTs and that the adsorption energy is stronger for bridge sites with lesser local curvature radii (R'), i.e. greater curvature. The adsorption is accompanied by a large transfer of charge from the carbon atoms in the bridge site to the adsorbed oxygen atom, and is likewise enhanced by greater curvature of the bridge site. These trends hold true for all SWCNT cases studied with the exception of the (5,0) SWCNT. This is most likely due to its small size, and despite its great surface curvature, interaction between carbon atoms affected the adsorption of the oxygen atom. Comparisons with the atomic adsorption of oxygen on a graphene sheet confirmed the beneficiary effect of surface curvature on the adsorption energy and charge transfer. We also found that the oxygen molecule interacts weakly with SWCNTs and is characteristic of physisorption. The interaction is mainly due to van der Waals forces. Just like in the case of atomic oxygen, greater surface curvature also enhances the adsorption energy and charge transfer, albeit to a lesser extent. The oxygen molecule remains too far away from the SWCNT surface for any significant charge transfer or interaction of molecular orbitals to occur. Nonetheless, surface curvature still enhances the physisorption process of the oxygen molecule in SWCNT as compared with graphene. The adsorption of oxygen on Fe-SWCNT was also investigated. The oxygen atom weakly adsorbs on the Fe-SWCNT compared to the pristine cases. Similarly, the presence of Fe resulted in lower chemisorption energies and energy barriers

for oxygen dissociation on SWCNT. Thus the presence of Fe enhances the oxygen reduction capabilities of SWCNT.

On the other hand, the H_2O_2 molecule interacts weakly with both pristine and Fe-filled SWCNT with low adsorption energies and an equilibrium distance of about 3.75 Å from the SWCNT surface. The chemisorption process can be described as follows: A rather negligible energy barrier was found, which is most likely due to the dissociation of the H_2O_2 molecule into hydroxyl pairs. These hydroxyl pairs attach to T-sites on the SWCNT surface, which increases the distance of the C-C bonds on the SWCNT surface. For the case of the semiconducting (3,3) Fe-filled SWCNT, the surface C-C bonds are completely destroyed. This result supports the assumption that the selective oxidation of semiconducting SWCNT found experimentally could also be applicable to Fe-filled SWCNT, and thus would also be important for purification of Fe-filled SWCNT with desired properties. Furthermore, the results of this study could be helpful in determining possible catalyst materials for oxygen reduction in the PEMFC.

Chapter 4

Summary and Recommendations

4.1   Synthesis of research results

DFT-based calculations were conducted to study the interaction of simple gas molecules (such as O, NO, and CO), with precious metal-free surfaces to provide an understanding of NO reduction and CO oxidation on Cu(111), CuO(110), and $Cu_2O(111)$ surfaces and explanations on the effects of surface curvature and the presence of Fe on the interaction of oxygen with SWCNTs.

Below are the key findings in relation to:
1   NO reduction and CO oxidation on copper oxide surfaces
    1.1   Strong molecular adsorption of NO was observed on the hollow sites of both CuO(110) and $Cu_2O(111)$ and have shown better reactivity than Cu(111).
    1.2   The Cu-terminated surfaces are preferred due to the presence of unsaturated surface Cu atoms, which form the active sites for NO dissociation. This is due to the modified electronic structure of the surface Cu atoms in the copper oxides wherein a shift of the d states towards the Fermi energy was observed as a result of the interaction with O atoms in the subsurface.
    1.3   Destabilization of the NO sigma bonds on the copper oxide surfaces promoted the easier dissociation of NO as the O atom separated and adsorbed on the adjacent hollow site. Furthermore, the excellent hybridization between the adsorbed NO molecule and the surface Cu led to the stability of the transition states for the case of the copper oxides, and the overall reaction was found to be exothermic.
    1.4   CO molecule adsorbed preferably on top of a surface Cu atom in the Cu-terminated surfaces. The adsorbed CO reacts with a coadsorbed O adatom, and not with a lattice O in an O-rich termination.

1.5   Molecularly adsorbed CO_2 is formed, while the overall reaction was found to be exothermic in copper oxides.

1.6   Reactivity of the copper oxide surface is enhanced with the presence of an electric field in the direction emanating from the surface. Stronger adsorption energy and greater amount of charge transfer is observed in the presence of electric field.

2   Interaction of oxygen with pristine and Fe-filled SWCNT

2.1   The oxygen atom is strongly chemisorbed on the bridge site of the SWCNTs and that the adsorption energy is stronger for bridge sites with lesser local curvature radii (R'), i.e. greater curvature.

2.2   The adsorption is accompanied by a large transfer of charge from the carbon atoms in the bridge site to the adsorbed oxygen atom, and is likewise enhanced by greater curvature of the bridge site.

2.3   These trends hold true for all SWCNT cases studied with the exception of the (5,0) SWCNT. This is most likely due to its small size, and despite its great surface curvature, interaction between carbon atoms affected the adsorption of the oxygen atom.

2.4   The oxygen molecule interacts weakly with SWCNTs and is characteristic of physisorption. The interaction is mainly due to van der Waals forces. Just like in the case of atomic oxygen, greater surface curvature also enhances the adsorption energy and charge transfer, albeit to a lesser extent.

2.5   The oxygen atom weakly adsorbs on the Fe-filled SWCNT compared to the pristine cases. This can be attributed to the modified electronic structure of the nanotube due to the effect of Fe. The surface carbon atoms in the vicinity of Fe have a depletion of occupied states near the Fermi level as compared to the surface C atoms of the pristine SWCNT.

2.6   Selective oxidation of SWCNT due to hydrogen peroxide was observed for Fe-filled SWCNT.

4.2   Outlook and recommendations for future research

The knowledge from theoretical investigations on these reactions is a good starting point for designing precious metal-free catalysts. Insights and trends obtained in this study can be used as the basis for looking for other potential catalyst materials. For instance, copper oxide surfaces are proposed as an alternative precious metal-free catalyst for possible application in the

three-way catalytic converter. In this study, it was shown that copper oxide surfaces exhibit excellent reactivity for both NO reduction and CO oxidation. Thus it can be recommended that copper oxides are potentially good catalysts for the three-way catalytic converter. Further DFT-based studies can be done to investigate the reactivity of the copper oxides for hydrocarbon oxidation, and finally to combine all three reactions that simultaneously occur in the catalytic converter. Moreover, this study confirms that the unsaturated Cu atoms on the surface provide the active site for NO reduction, and that CO reacts with the adsorbed O atoms instead of lattice O atoms for CO oxidation. These insights can be used for future catalyst design. To promote the presence of active sites and enhance the reactivity of the catalyst surface, the introduction of vacancies, as well as co-doping of different metals or metal oxides can be done to reproduce the same effects that produce such active sites.

For the case of the interaction of oxygen with SWCNTs, it was shown that greater surface curvature enhances the adsorption energy and charge transfer for oxygen adsorption. On the other hand, while the presence of Fe inside SWCNTs results in a slightly weaker oxygen adsorption, the energy barrier for O_2 dissociation is reduced and Fe-filled SWCNTs are resistant to oxidation from H_2O_2 poisoning. By combining the effect of surface curvature and Fe-filling, the reactivity of SWCNTs with oxygen can be increased and its durability towards H_2O_2 poisoning improved. These findings open numerous possibilities for future catalyst design for oxygen reduction in the PEMFC. For instance, Fe-filled SWCNTs can be decorated with other metals on the surface to further enhance its oxygen reduction capabilities. Due to the resistance to H_2O_2 poisoning, pathways for oxygen reduction that involve peroxide intermediates may be explored in future studies.

Appendix

Density Functional Theory and Implementation

The Density Functional Theory (DFT) is a quantum mechanical method used in physics and chemistry to investigate the electronic structure of many-body systems, in particular molecules and condensed phases. Superconductivity, atoms in the focus of strong laser pulses, relativistic effects in heavy elements and in atomic nuclei, classical liquids, binding energy of molecules, band structure of solids, and magnetic properties of alloys have all been studied using DFT. DFT owes its versatility to the generality of its fundamental concepts and the flexibility one has in implementing them. It has two core elements: the Hohenberg-Kohn theorem and the Kohn-Sham equations. [110]

All information that can possibly be obtained about a given system is contained in the system's wave function, Ψ. In dealing with the electronic structure of atoms, molecules, and solids, the nuclear degrees of freedom (e.g., the crystal lattice in a solid) appear in the form of a potential $v(\mathbf{r})$ acting on the electrons, thus the wave function depends only on the electronic coordinates. Nonrelativistically, this wave function is calculated from the Schrödinger equation for a single electron moving in a potential $v(\mathbf{r})$. For cases of more than one electron (i.e., one has a many-body problem), the Schrödinger's equation is modified by including the electron-electron interaction, $U(\mathbf{r}_i, \mathbf{r}_j)$. It is only through $\hat{U}$ that the single-body quantum mechanics differs from the extremely complex many-body problem.

The usual quantum-mechanical approach to Schrödinger equation can be summarized by the following sequence: (1) One specifies the system by choosing $v(\mathbf{r})$, (2) Plug $v(\mathbf{r})$ into the Schrödinger equation, (3) Solve the Schrödinger equation for the wave function Ψ, and (4) Calculate expectation values of observables for Ψ. One of the observables calculated in this way is the particle density $n(\mathbf{r})$.

Many powerful methods for solving the Schrödinger equation for many-body systems have been developed, such as the diagrammatic perturbation theory in physics (based on Feynman diagrams and Green's functions), while in chemistry one uses configuration interaction (CI) methods (based on systematic expansion in Slater determinants). But it is simply impossible to apply them efficiently to large and complex systems. DFT provides a viable and more versatile, though less accurate alternative. It explicitly recognizes that the nonrelativistic Coulomb systems differ only by their potential $v(\mathbf{r})$. Moreover, it provides a way to systematically map the many-body problem, with $\hat{U}$, onto a single-body problem, without $\hat{U}$. This is done by making $n(\mathbf{r})$ the key variable on which the calculation of other observables can be based. The extent to which DFT has contributed to science is reflected by the 1998 Nobel Prize in Chemistry awarded to Walter Kohn, the founding father of DFT, and John Pople, who was instrumental in implementing DFT in chemistry.

The density-functional approach can be summarized by the following sequence: (1) Knowledge of $n(\mathbf{r})$ implies knowledge of Ψ, and $v(\mathbf{r})$, and (2) All other observables can be obtained.

At the heart of the Density Functional Theory is the Hohenberg-Kohn (HK) theorem. In simplest terms, the HK theorem is as follows: *Given a ground-state density $n_o(\mathbf{r})$ it is possible to calculate the corresponding ground-state wave function Ψ_o ($\mathbf{r}_1$, $\mathbf{r}_2$..., $\mathbf{r}n$).* This means that Ψ_o is a functional of n_o. It therefore follows that all ground-state observables are functionals of n_o too. Knowledge that a given function is a ground-state density implies the knowledge of an extremely detailed subsidiary condition: this function represents the spatial distribution of probability of the lowest energy solution to the Schrödinger equation.

In summary, the HK theorem consists of the following: (1) The ground-state wave function is a unique functional of the ground-state density: $\Psi_o = \Psi[n_o]$. Consequently, the ground-state expectation value of any observable is also functional of $n_o(\mathbf{r})$. (2) The ground-state energy has a useful variational property: $E_v[n_o] \leq E_v[n']$, which means that if the ground-state energy of a Hamiltonian is calculated using a density that is not its ground-state density, a result below the true ground-state energy cannot be found. (3) Once the system is specified, the functional $V[n]$ is known explicitly.

$$V[n] = \int d^3r\, n(\mathbf{r})v(\mathbf{r})$$

Finally, (4) the ground-state energy also determines the potential $v(\mathbf{r})$. This holds true if DFT is

formulated exclusively in terms of charge density. [32]

The minimization of an explicit energy functional is not normally the most efficient implementation of DFT. Much more widely used is the Kohn-Sham approach, which does not exclusively work in terms of the particle (or charge) density, but involves a special kind of wave functions (single-particle orbitals).

An effective way to treat the kinetic energy functional is based on decomposing $T[n]$ into one part that represents the kinetic energy of noninteracting particles, $T_s[n]$, and one that represents the remainder, $T_c[n]$. (the subscripts s and c stand for 'single-particle' and 'correlation' respectively)

$$T[n] = T_s[n] + T_c[n]$$

$T_s[n]$ can be expressed in terms of the single-particle orbitals $\phi_i(r)$ of a noninteracting system with density n. This is because the total kinetic energy for noninteracting particles is just the sum of the individual kinetic energies.

$$T_s[n] = -\frac{\hbar^2}{2m} \sum_i^N \int d^3r \phi_i^*(r) \nabla^2 \phi_i(r)$$

Since all $\phi_i(r)$ are functionals of n, this expression for T_s is an explicit orbital function but an implicit density functional, $T_s[n] = Ts[\{\phi_i[n]\}]$. The exact energy functional can now be rewritten as

$$E[n] = T[n] + U[n] + V[n] = T_s[\{\phi_i[n]\}] + U_H[n] + E_{xc}[n] + V[n]$$

$E_{xc}[n]$ is known as the exchange-correlation energy. It is often decomposed as $E_{xc} = E_x + E_c$, where E_x is due to the Pauli principle (exchange energy) and E_c is due to correlations. (T_c is then part of E_c.) The exchange energy can be written explicitly in terms of the single-particle orbitals.

$$E_x[\{\phi_i[n]\}] = -\frac{q^2}{2} \sum_{jk} \int d^3r \int d^3r' \frac{\phi_j^*(r)\phi_k^*(r')\phi_j(r')\phi_k(r)}{|r - r'|}$$

Clearly E_c is an enormously complex object. However, the practical advantage of writing $E[n]$

in the form above is that the unknown functional $E_{xc}[n]$ is typically much smaller than the known terms T_s, U_H, and V. Therefore, reasonably simple approximations for $E_{xc}[n]$ could provide useful results for $E[n]$. Two properties of the exchange, $E_x[n]$, and correlation, $E_c[n]$, contributions to this functional are the scaling conditions obtained by Levy and Perdew.

$$E_x[n_\lambda] = \lambda E_x[n]$$
$$E_c[n_\lambda] > \lambda E_c[n] \qquad \text{for } \lambda > 1$$
$$E_c[n_\lambda] < \lambda E_c[n] \qquad \text{for } \lambda < 1$$

$n\lambda(\boldsymbol{r}) = \lambda^3 n(\lambda \boldsymbol{r})$ is a scaled density. [33]

Presented below is a scheme suggested by Kohn and Sham for performing the minimization indirectly.

$$0 = \frac{\delta E[n]}{\delta n(\boldsymbol{r})} = \frac{\delta T_s[n]}{\delta n(\boldsymbol{r})} + \frac{\delta V[n]}{\delta n(\boldsymbol{r})} + \frac{\delta U_H[n]}{\delta n(\boldsymbol{r})} + \frac{\delta E_{xc}[n]}{\delta n(\boldsymbol{r})} = \frac{\delta T_s[n]}{\delta n(\boldsymbol{r})} + v(\boldsymbol{r}) + v_H(\boldsymbol{r}) + v_{xc}(\boldsymbol{r})$$

Now consider a noninteracting system of particles moving in an external potential $v_s(\boldsymbol{r})$. The minimization simply becomes

$$0 = \frac{\delta E_s[n]}{\delta n(\boldsymbol{r})} = \frac{\delta T_s[n]}{\delta n(\boldsymbol{r})} + \frac{\delta V_s[n]}{\delta n(\boldsymbol{r})} = \frac{\delta T_s[n]}{\delta n(\boldsymbol{r})} + v_s(\boldsymbol{r})$$

Notice that both minimizations have the same solution $n_s(\boldsymbol{r}) \equiv n(\boldsymbol{r})$ if $v_s(\boldsymbol{r})$ is chosen to be

$$v_s(\boldsymbol{r}) = v(\boldsymbol{r}) + v_H(\boldsymbol{r}) + v_{xc}(\boldsymbol{r})$$

The density of the interacting (many-body) system in potential $v(\boldsymbol{r})$ can now be calculated by solving the equations of a noninteracting (single-body) system in potential $v_s(\boldsymbol{r})$.

$$\left[-\frac{\hbar^2 \nabla^2}{2m} + v_s(\boldsymbol{r}) \right] \phi_i(\boldsymbol{r}) = \epsilon_i \phi_i(\boldsymbol{r})$$

This yields orbitals that produce the density $n(\boldsymbol{r})$ of the original system.

$$n(\boldsymbol{r}) \equiv n_s(\boldsymbol{r}) = \sum_{i}^{N} f_i |\phi_i(\boldsymbol{r})|^2$$

The latter three equations are the celebrated Kohn-Sham (KS) equations. They replace the problem of minimizing *E[n]* by that of solving a noninteracting Schrödinger equation. Both v_H and v_{xc} depend on *n*, which depends on ϕ_i, which in turn depends on v_s. the problem of solving the KS equations is a nonlinear one. Start first with an initial guess for *n(r)*, calculate the corresponding $v_s(\boldsymbol{r})$, and then solve for ϕ_i. Then a new density is calculated, and then used to start again. The process is repeated until it converges (self-consistency cycle). [33]

The electron orbitals used to express the single particle density may be expanded in terms of any converged basis set. In practice a plane wave basis set is used as this confers a number of benefits. A plane wave basis set is unbiased; it does not assume any preconceptions of the form of the problem. Due to Bloch's theorem plane waves are the natural choice for the representation of electron orbitals in a periodic system. The kinetic energy operator is diagonal in a plane wave representation. Similarly the potential is diagonal in real space. The use of Fast Fourier Transforms in changing between these representations provides a large saving in computational cost. As a plane wave basis set is non-local no Pulay forces will arise when calculating the forces on the ions in the system. Hence these ionic forces may be calculated with greater efficiency.

The principle disadvantage of a plane wave basis set is its inefficiency. The number of basis functions needed to describe atomic wavefunctions accurately near to a nucleus would be prohibitive. This difficulty is overcome by the use of Pseudopotentials to represent the potential of the ionic cores. This approximation makes the assumption that only the valence electrons determine the physical properties of the system. The pseudopotential represents the potential of the nucleus and the core electrons subject to the following conditions. (1) The valence wavefunction remains unchanged outside the core region. (2) The pseudowavefunction within the core matches correctly at the boundary. (3) The phase shift caused by the core is unchanged. And (4), the norm of the valence wavefunction in the core is unchanged.

The use of plane waves as a basis set may only be applied to a system exhibiting three-dimensional translational symmetry. An aperiodic system would require a continuous plane wave basis set and hence an infinite number of plane wave basis functions. This limitation may be overcome by embedding an aperiodic system such as a molecule in a periodic system of supercells. Provided the supercell is sufficiently large that the interactions between the

molecules are negligible, the energy per supercell will be identical to that of a single molecule. If the energy per supercell has converged sufficiently with respect to supercell size the interaction between molecules will be negligible.

Acknowledgments

I would also like to thank the following who have been part of the success of this research:

To my supervisor, Prof. Hideaki Kasai for his utmost guidance and mentoring every step of the way, for always supporting me and most of all, for being considerate and understanding of my circumstances;

To Dr. Wilson Agerico Diño for his guidance, valuable insights and discussions, and for always pushing me to do my best;

To Dr. Hiroshi Nakanishi for assistance in computations and networking, especially the technicalities;

To the reviewers of this dissertation, Prof. Yoshitada Morikawa, Prof. Michio Okada, Dr. Koichi Kusakabe, and Dr. Koun Shirai, for the meetings and discussions;

To Prof. Hiroshi Ajiki through the CNT-NE project for the opportunity to attend many conferences and meet the experts in the CNT research field;

To the staff of the Kasai Laboratory, for all the support and assistance, especially for paperwork and for making the lives of us students easier and worry-free;

To Ate Mel, Ate Clare, Ate Susan, Tanglaw, and Allan, for their guidance and mentoring, and for being my good "sempais" in the lab;

To all the students in Kasai Lab, then and now, for making life in the lab interesting and exciting;

To the Filipino Students Society in Osaka (FilSSO), International Youth Group (IYG), and San Lorenzo Ruiz Filipino-Japanese community (SLRFJ), my family here in Japan, for all the support and the good times;

To my parents and family for their loving support in everything that I do, they have served as my inspiration to do the best that I can in all endeavors I encounter;

And last but most important of all, to Almighty God, the Divine Providence, our Father and Creator, for the talents and abilities He has given me, without which, none of this could be possible.

References

[1] J. Wintterlin, S. Volkening, T.V.W. Janssens, T. Zambelli, and G. Ertl. Atomic and Macroscopic Reaction Rates of a Surface-Catalyzed Reaction. *Science* 278 (1997) 1931.

[2] D. Loffreda, D. Simon, and P. Sautet. Structure sensitivity for NO dissociation on palladium and rhodium surfaces. *J. Catal.* 213 (2003) 211-25.

[3] A. Dicks. The role of carbon in fuel cells. *Power Sources* 152 (2006) 128-41.

[4] W.A. Brown and D.A. King. NO chemisorption and reactions on metal surfaces: a new perspective *J. Phys. Chem. B* 104 (2000) 2578–95.

[5] F. Garin. Mechanism of NO_x decomposition. *Appl. Catal. A* 222 (2001) 183-219.

[6] Z.P. Liu and P. Hu. CO oxidation and NO reduction on metal surfaces: density functional theory investigations. *Topics in Catalysis* 28 (2004) 71-8.

[7] J Novakova. Reduction of NO by hydrogen versus reduction by CO over Pt, Pd and Rh clusters in NaX zeolite. *Appl. Catal B* 30 (2001) 445-57.

[8] B. Hammer. The NO + CO reaction catalyzed by flat, stepped, and edged Pd surfaces. *J. catal*. 199 (2001) 171-6.

[9] F. Oemry, M.C. Escaño, H. Kishi, S. Kunikata, H. Nakanishi, H. Kasai, H. maekawa, K. Osumi, and Y. Tashiro. Nitrogen monoxide adsorption on Pt4 clusters coated on γAl_2O_3 (111) surface. *J. Nanosci. Nanotechnol*. 11 (2011) 2844-50.

[10] A. Alavi, P. Hu, T. Deutsch, P.L. Silvestrelli, and J. Hutter. CO oxidation on Pt(111): an *ab-initio* density functional theory study. *Phys. Rev. Lett.* 80 (1998) 3650-3.

[11] H. Over, Y.D. Kim, A.P. Seitsonen, S. Wendt, E. Lundgren, M. Schmid, P. Varga, A. Morgante, and G. Ertl. Atomic-scale structure and catalytic reactivity of the RuO2(110) surface. *Science*. 287 (2000) 1474-6.

[12] M.J.P. Hopstaken and J.W. Niemantsverdriet. Structure sensitivity in the CO oxidation on rhodium: Effect of adsorbate coverages on oxidation kinetics on Rh(100) and Rh(111). *J. Chem. Phys.* 113 (2000) 5457-65.

[13] A. Eichler. 2001. CO oxidation on transition metal surfaces: reaction rates from first principles. *Surf. Sci.* 498 (2001) 314-20.

[14] X.-Q. Gong, Z.-P. Liu, R. Raval, and P. Hu. A systematic study of CO oxidation on metals and metal oxides: density functional theory calculations. *J. Am. Chem. Soc.* 126 (2004) 8-9.

[15] A.K. Santra and D.W. Goodman. Catalytic oxidation of CO by platinum group metals: from ultrahigh vacuum to elevated pressures. *Electrochim. Acta.* 47 (2002) 3595-609.

[16] N. Lopez and J.K. Norskov. Synergetic effects in CO adsorption on Cu-Pd (111) alloys. *Surf. Sci.* 477 (2001) 59-75.

[17] L. Petrov, J. Soria, L. Dimitrov, R. Cataluna, L. Spasov, and P. Dimitrov. Cu exchanged microporous titanium silicate (TS-1) coated on polycrystalline mullite fibres as catalyst for CO and NO conversion. *Appl. Catal. B* 8 (1996) 9.

[18] X. Courtois and V. Perrichon. Distinct roles of copper in bimetallic copper-rhodium three-way catalysts deposited on redox supports. Appl. Catal. B 57 (2005) 63.

[19] M.H. Matloob, M.W. Roberts. Electron spectroscopic study of nitrogen species adsorbed on copper. *J. Chem. Soc., Faraday Trans.* 73 (1977) 1393.

[20] D.W. Johnson, M.H. Matloob, M.W. Roberts. Study of the interaction of nitric oxide with Cu (100) and Cu (111) surfaces using low energy electron diffraction and electron spectroscopy. *J. Chem. Soc., Faraday Trans.* 75 (1979) 2143.

[21] P. Dumas, M. Suhren, Y.J. Chabal, C.J. Hirschmugl, G.P. Williams. Adsorption and reactivity of NO on Cu(111): a synchrotron infrared reflection absorption spectroscopic study. *Surf. Sci*. 371 (1997) 200.

[22] S. Gonzalez, C. Sousa and F. Illas. Promoter and poisoning effects on NO-catalyzed dissociation on bimetallic RhCu(111) surfaces. *J. Catal.* 239 (2006) 431-40.

[23] M. Yen and J. Ho. Density-functional study for NO_x (x = 1, 2) dissociation mechanism on the Cu (111) surface. *Chem. Phys.* 373 (2010) 300-6.

[24] S. Gonzalez, C. Sousa, and F. Illas. Similarities and differences on the molecular mechanism of CO oxidation on Rh(111) and bimetallic RhCu(111) surfaces. *Phys. Chem. Chem. Phys.* 9 (2007) 2877-85.

[25] M. Manzoli, R. Di Monte, F. Boccuzzi, S. Coluccia, and J. Kaspar. CO oxidation over CuO_x-CeO_2-ZrO_2 catalysts: Transient behavior and role of copper clusters in contact with ceria. *Appl. Catal. B.* 61 (2005) 192-205.

[26] G. Aguila, F. Gracia, and P. Araya. CuO and CeO_2 catalysts supported on Al_2O_3, ZrO_2, and SiO_2 in the oxidation of CO at low temperature. *Appl. Catal. A.* 343 (2008) 16-24.

[27] B. White, M. Yin, A. Hall, D. Le, S. Stolbov, T. Rahman, N. Turro, and S. O'Brien. Complete CO oxidation over Cu_2O nanoparticles supported on silica gel. *Nano Lett.* 6 (2006) 2095-8.

[28] S. Sun, Y. Sun, X. Zhang, H. Zhang, X. Song and Z. Yang. A surfactant-free strategy for controllable growth of hierarchical copper oxide nanostructures. *CrystEngComm* 15 (2013) 5275.

[29] M. Mahinroosta. Catalytic effect of commercial nano-CuO and nano-Fe_2O_3 on thermal decomposition of ammonium perchlorate. *J. Nanostruct. Chem.* 3 (2013) 47.

[30] R. H. Bari, S. B. Patil and A. R. Bari. Spray-pyrolized nanostructured CuO thin films for H2S gas sensor. *Int. Nano Lett.* 3 (2013) 12.

[31] W. Xiang, J. Liu, M. Chang and C. Zheng. The adsorption mechanism of elemental mercury on CuO(110) surface, *Chem. Eng. J.* 200 (2012) 91.

[32] P. Hohenberg and W. Kohn. Inhomogeneous electron gas. *Phys. Rev.* 136 (1964) B864.

[33] W. Kohn and L. Sham. Self-consistent equations including exchange and correlation effects. *Phys. Rev.* 140 (1965) A1133.

[34] G. Kresse and J. Furthmuller. Efficiency of ab-initio total energy calculations for metals and semiconductors using a plane-wave basis set. *Comput. Mater. Sci.* 6 (1996) 15.

[35] G. Kresse and J. Furthmuller. Efficient iterative schemes for ab-initio total-energy calculations using a plane-wave basis set. *Phys. Rev.* B 54 (1996) 11169.

[36] P.E. Blochl. Projector augmented-wave method. *Phys. Rev.* B 50 (1994) 17953.

[37] J.P. Perdew, K. Burke and M. Ernzerhof. Generalized gradient approximation made simple. *Phys Rev Lett*, 77 (1996) 3865.

[38] J.P. Perdew, K. Burke and M. Ernzerhof. Generalized gradient approximation made simple. *Phys. Rev. Lett.* 78 (1996) 1396.

[39] S. Grimme. Semiempirical GGA-type density functional construed with a long-range dispersion correction. *J. Comput. Chem.* 25 (2004) 1463.

[40] J.B. Forsyth and S. Hull. The effect of hydrostatic pressure on the ambient temperature structure of CuO. *J. Phys.: Condens. Matter* 3 (1991) 5257.

[41] A. Migani and F. Illas. A Systematic Study of the Structure and Bonding of Halogens on Low-Index Transition Metal Surfaces. *J. Phys. Chem.* B 110 (2006) 11894.

[42] E. Ruiz, S. Alvarez, P. Alemany, and R. Evarestov. Electronic structure and properties of Cu2O. *Phys. Rev.* B 56 (1997) 7189-96.

[43] N.W. Ashcroft and N.D. Mermin. *Solid State Physics* (Thomson Learning, New York, 1976)

[44] H. Monkhorst and J. Pack. Special points for Brillouin zone integration. *Phys. Rev.* B 1976 **56** 7189.

[45] G. Henkelman, B. P. Uberuaga and H. Jonsson. A climbing image nudged elastic band method for finding saddle points and minimum energy paths. *J. Chem. Phys.* 113 (2000) 9901.

[46] P. Maragakis, S. A. Andreev, Y. Brumer, D. R. Reichman and E. Kaxiras. Adaptive nudged elastic band approach for transition state calculation. *J. Chem. Phys.* 117 (2002) 4651.

[47] M. Gajdos, J. Hafner and A. Eichler. CO adsorption on close-packed transition and noble metal surfaces: Trends from ab-initio calculations. *J. Phys.: Condens. Matter* 18 (2006) 4.

[48] M.A. van Daelan, Y.S. Li, J.M. Newsam, and R.A. van Santen. Energetics and dynamics of NO and CO dissociation on Cu(100) and Cu(111). *J. Phys. Chem.* 100 (1996) 2279-89.

[49] O.R. Gilliam, C.M. Johnson and W. Gordy, Microwave Spectroscopy in the Region from Two to Three Millimeters. *Phys. Rev.* 78 (1950) 140.

[50] J. Frese. Electrochemical Reduction of CO_2 at Intentionally Oxidized Copper Electrodes. *J. Electrochem. Soc.* 138 (1991) 3338.

[51] M. Le, M. Ren, Z. Zhang, P. T. Sprunger, R. L. Kurtz, and J. C. Flake. Electrochemical Reduction of CO_2 to CH_3OH at Copper Oxide Surfaces. *J. Electrochem. Soc.* 158 (2011) E45-9.

[52] G. Ghadimkhani, N. R. Tacconi, W. de Chanmanee, C. Janaky, and K. Rajeshwar. Efficient solar photoelectrosynthesis of methanol from carbon dioxide using hybrid CuO–Cu_2O semiconductor nanorod arrays. *Chem. Commun.* 49 (2013) 1297.

[53] H. Wu, N. Zhang, Z. Cao, H. Wang, and S. Hong. The adsorption of CO_2, H_2CO_3, HCO^{3-} and CO_3^{2-} on Cu_2O (111) surface: First-principles study. *Int. J. Quantum Chem.* 112 (2012) 2532.

[54] H. Wu, N. Zhang, H. Wang, and S. Hong. Adsorption of CO_2 on Cu_2O (111) oxygen-vacancy surface: First-principles study. *Chem. Phys. Lett.* 568-569 (2013) 84.

[55] L.I. Bendavid and E.A. Carter. CO_2 Adsorption on $Cu_2O(111)$: A DFT+U and DFT-D Study. *J. Phys. Chem. C.* 117 (2013) 26048.

[56] G. Herzberg, *Electronic spectra and electronic structure of polyatomic molecules* (Van Nostrand, New York, 1966).

[57] H. Aizawa, Y. Morikawa, S. Tsuneyuki, K. Fukutani, T. Ohno. A density-functional study of the atomic structures and vibrational spectra of NO/Pt (111). *Surf. Sci.* 514 (2002) 394.

[58] N. Kruse, G. Abend, J.H. Block. The kinetics of adsorption and thermal desorption of NO on stepped Pt single crystal surfaces. *J. Chem. Phys.* 88 (1988) 1307.

[59] H.J. Kreuzer, L.C. Wang. Field‐induced surface chemistry of NO. *J. Chem. Phys.* 93 (1990) 6065.

[60] J. Neugebauer, M. Scheffler. Adsorbate-substrate and adsorbate-adsorbate interactions of Na and K adlayers on Al(111). *Phys. Rev. B.* 46 (1992) 16067.

[61] S. Iijima. Helical microtubules of graphitic carbon. *Nature.* 354 (1991) 56.

[62] T. Ebbesen: Carbon Nanotubes: Preparation and Properties. (CRC Press, Inc, Boca Raton, 1997).

[63] E. Lafuente, E. Munoz, A.M. Benito, W.K. Maser, M.T. Martinez, F. Alcaide, L. Ganborena, I. Cendoya, O. Miguel, J. Rodriguez, E.P. Urriolabeitia, R. Navarro. Single-walled carbon nanotube supported platinum nanoparticles as fuel cell electrocatalysts. *J Mater Res,* 21 (2006) 2841-6.

[64] Girishkumar G, Vinodgopal K, Kamat P. Carbon nanostructures in portable fuel cells: single-walled carbon nanotube electrodes for methanol oxidation and oxygen reduction. *J Phys Chem B,* 108 (2004) 19960-6.

[65] X. Wang, W. Li, Z. Chen. M. Waje, Y. Yan. Durability investigation of carbon nanotube as catalyst support for proton exchange membrane fuel cell. *J. Power Sources.* 158 (2006) 154.

[66] J. Liu, A.G. Rinzler, H. Dai, J.F. Hafner, R. Kelley Bradley, P.J. Boul, A. Lu, T. Iverson, K

Shelimov, C. Huffman, et al. Fullerene Pipes. *Science* 280 (1998) 1253.

[67] E.W. Wong, P.E. Sheehan, C.M. Lieber. Nanobeam Mechanics: Elasticity, Strength, and Toughness of Nanorods and Nanotubes. *Science* 277 (1997) 1971.

[68] S. Saito. Carbon nanotubes for next-generation electronic devices. *Science* 278 (1997) 77.

[69] S.J. Tans, M.H. Devoret, H. Dai, A. Thess, R.E. Smalley, L.J. Geerligs, C. Dekker. Inidvidual single-wall carbon nanotubes as quantum wires. *Nature* 386 (1997) 474.

[70] J.T. Hu, M. Ouyang, P. Yang, C.M. Lieber. Controlled growth and electrical properties of heterojunctions of carbon nanotubes and silicon wires. *Nature* 399 (1999) 48.

[71] S.J. Tans, A.R.M. Verschueren, C. Dekker. Room-temperature transistor based on a single carbon nanotube. *Nature* 393 (1998) 49.

[72] M. Kisaku, M.D.M. Rahman, T. Kishi, D. Matsunaka, T.A. Roman, W.A. Diño, H. Nakanishi, H. Kasai. Diameter dependent magnetic and electronic properties of single-walled carbon nanotubes with Fe nanowires. *Jpn J Appl Phys*, 44 (2005) 882-8.

[73] M. David, T. Kishi, M. Kisaku, H. Nakanishi, H. Kasai. Carbon nanoarch encapsulating Fe nanowire on Ni(111). *Jpn J Appl Phys*, 45 (2006) 2869-71.

[74] M. David, K. Kasai, J. Moreno, H. Kasai. Understanding the bond-making and bond-breaking of Fe-filled SWNT on Ni(111). *Surf Interface Anal*, 40 (2008), 1098-102.

[75] J. Xie, D. Wood, D. Wayne, T. Zawodzinski, P. Atanassov, R. Borup. Durability of PEFCs at high humidity conditions. *J Electrochem Soc,* 152 (2005), A104-13.

[76] M. Mathias, et al: Abstr. Pap. Am. Chem. Soc. 228 (2004) U653

[77] S.D. Knights, et al: J. Power Sources 127 (2004) 127.

[78] D.A. Stevens and J.R. Dahn: Carbon 43 (2005) 179

[79] A. Taniguchi, et al: J. Power Sources 130 (2004) 42

[80] K. Kangasniemi, D. Condit, T. Jarvi. Characterization of Vulcan electrochemically oxidized under simulated PEM fuel cell conditions. *J Electrochem Soc*, 151 (2004), E125-32.

[81] L. Roen, C. Paik, T. Jarvi. Electrocatalytic corrosion of carbon support in PEMFC cathodes. *Electrochem Solid-State Lett*, 7 (2004), A19-22.

[82] P.G. Collins, K. Bradley, M. Ishigami, A. Zettl. Extreme oxygen sensitivity of electronic properties of carbon nanotubes. *Science*, 287 (2000) 1801-4.

[83] K.A. Dean, B.R. Chalamala. Current saturation mechanisms in carbon nanotube field emitters. *Appl Phy Lett*, 76 (2000), 375.

[84] D. Kang, N. Park, J. Ko, E. Bae, W. Park. Oxygen-induced p-type doping of long individual single-walled carbon nanotube. *Nanotechnology*, 16 (2005) 1048.

[85] P. Ajayan, T. Ebbesen, T. Ichihashi, S. Iijima, K. Tanigaki, H. Hiura. Opening carbon nanotubes with oxygen and implications for filling. *Nature*, 362 (1993), 522-5.

[86] T. Ebbesen, P. Ajayan, H. Hiura, K. Tanigaki. Purification of nanotubes. *Nature*, 367 (1994) 519.

[87] M. Barberio, P. Barone, A. Bonanno, F. Xu. Oxygen interaction with single-walled carbon nanotubes. *Superlattice Microst*, 46 (2090), 365-8.

[88] T. Kawai, Y. Miyamoto. Chirality-dependent C-C bond breaking of crabon nanotubes by cyclo-addition of oxygen molecule. *Chem Phys Lett*. 453 (2008) 256-60.

[89] Z.M. Li. Polarized adsorption spectra of 4 Å carbon nanotubes aligned in channels of an AlPO4-5 single crystal, *Phys Rev Lett*. 87 (2001) 127401.

[90] J.T. Ye, Z.K. Tang. Raman spectra and thermal stability analysis of 0.4nm freestanding single-walled carbon nanotubes, *Phys Rev B*, 72 (2005) 045414.

[91] A. Ishii, M. Yamamoto, H. Asano, K. Fujiwara. DFT calculation for adatom adsorption on graphene sheet as a prototype for carbon nanotube functionalization. *J Phys: Conf Ser.* 100

(2008), 052087.

[92] P. Giannozzi, R. Car, G. Scoles. Oxygen adsorption on graphite and nanotubes, *J Chem Phys.* 118 (2003) 1003-6.

[93] S. Dag, O. Gulseren, T. Yildirim, S. Ciraci. Oxygenation of carbon nanotubes: Atomic structure, energetic, and electronic structure, *Phys Rev B.* 67 (2003) 165424.

[94] Y. Miyata, Y. Maniwa, H. Kataura. Selective oxidation of semiconducting single-wall carbon nanotubes by hydrogen peroxide. J. Phys. Chem. B 110 (2006) 25.

[95] B Pilas, T. Sarna, B. Kalyanaraman, H.M. Swartz. The effect of melanin on iron associated decomposition of hydrogen peroxide. *Free Radic. Biol. Med.* 4 (1988) 285.

[96] O. Antoine, R. Durand. RRDE study of oxygen reduction on Pt nanoparticles inside Nafion®: H2O2 production in PEMFC cathode conditions. *J. Appl. Electrochem.* 30 (2000) 839.

[97] N.M. Markovic, T.J. Schmidt, V. Stamenkovic, P.N. Ross. Oxygen Reduction Reaction on Pt and Pt Bimetallic Surfaces: A Selective Review. *Fuel Cells* 1 (2001) 105.

[98] I. Morcos, E. Yeager. Kinetic studies of the oxygen—peroxide couple on pyrolytic graphite. *Electrochim. Acta* 15 (1970) 953.

[99] L. Zhang, S. Mukerjee. Investigation of Durability Issues of Selected Nonfluorinated Proton Exchange Membranes for Fuel Cell Application. *J. Electrochem. Soc.* 153 (2006) A1062.

[100] J. Qiao, M. Saito, K. Hayamizu, T. Okada. Degradation of Perfluorinated Ionomer Membranes for PEM Fuel Cells during Processing with H_2O_2. *J. Electrochem. Soc.* 153 (2006) A967.

[101] W. Liu, D. Zuckerbrod. *In Situ* Detection of Hydrogen Peroxide in PEM Fuel Cells. *J. Electrochem. Soc.* 152 (2005) A1165.

[102] S.D. Knights, K.M. Colbow, J. ST-Pierre, D.P. Wilkinson. Aging mechanisms and lifetime of PEFC and DMFC. *J. Power Sources* 127 (2004) 127.

[103] M. Pianca, E. Barchiesi, G. Esposto, S. Radice. End groups in fluoropolymers. *J. Fluorine Chem.* 95 (1999) 71.

[104] C. Espro, G. Bonura, F. Arena, F. Frusteri, A. Parmaliana, F. Sini, V. Solinas. Factors affecting the efficiency of Nafion-based catalytic membranes in the selective oxidation of light paraffins mediated by the Fenton system. *Catal. Today* 91 (2004) 215.

[105] A. Pozio, R.F. Silva, M. De Francesco, L. Giorgi. Nafion degradation in PEFCs from end plate iron contamination. *Electrochim. Acta* 48 (2003) 1543.

[106] F. Frusteri, C. Espro, F. Arena, E. Passalacqua, A. Patti. A. Parmaliana. Partial oxidation of propane on Nafion supported catalytic membranes. *Catal. Today* 61 (2000) 37.

[107] C. Espro, F. Frusteri, F. Arena, A. Parmaliana. Selective oxidation of propane on a Nafion-based catalytic membrane mediated by Fe^{II}–H$_2$O$_2$ Fenton system. *J. Mol. Catal*. A 159 (2000) 359.

[108] T. Yuranova, O Enea, E. Mielczarski, J. Mielczarski, P. Albers, J. Kiwi. Fenton immobilized photo-assisted catalysis through a Fe/C structured fabric. *Appl. Catal.* B 49 (2004) 39.

[109] U.H. Jung, S.U. Jeong. K. Chun, K.T. Park, H.M. Lee, D.W. Choi, S.H. Kim. Reduction of hydrogen peroxide production at anode of proton exchange membrane fuel cell under open-circuit conditions using ruthenium–carbon catalyst. *J. Power Sources* 170 (2007) 281.

[110] K. Capelle. (2002). A Bird's Eye-view of Density Functional Theory. arXiv:cond-mat/0211443.

Publications

1. A. Padama, H. Kishi, R. Arevalo, J. Moreno, H. Kasai, M. Taniguchi, M. Uenishi, H. Tanaka, and Y. Nishihata. "NO dissociation on Cu(111) and $Cu_2O(111)$ surfaces: a density functional theory based study," *Journal of Physics: Condensed Matter*, 24 (2012) 175005-175010.

2. H. Kishi, A. Padama, R. Arevalo, J. Moreno, H. Kasai, M. Taniguchi, M. Uenishi, H. Tanaka, and Y. Nishihata. "A theoretical study of the reactivity of $Cu_2O(111)$ surfaces: the case of NO dissociation" *Journal of Physics: Condensed Matter*, 24 (2012) 262001-262005.

3. Ryan Lacdao Arevalo, Hirofumi Kishi, Allan Abraham Bustria Padama, Joaquin Lorenzo Valmoria Moreno, Hideaki Kasai. "Substrate dependence of Pt_4 electronic properties," *Journal of Physics: Condensed Matter*, 25 (2013) 222001.

4. Joaquin Moreno, Melanie David, Hideaki Kasai. "Interaction of Oxygen With Fe Nanowire-Filled Single-Walled Carbon Nanotubes", *Advances in Natural Science*, 6 (2013) 1-5.

5. Joaquin Lorenzo Valmoria Moreno, Allan Abraham Bustria Padama, Hideaki Kasai . "A density functional theory-based study on the dissociation of NO on CuO(110) surface" CrystEngComm, 16 (2014) 2260-2265.

6. Joaquin Lorenzo Valmoria Moreno, Ryan Lacdao Arevalo, Mary Clare Sison Escano, Allan Abraham Bustria Padama, Hideaki Kasai. "A Theoretical Study on the Adsorption of CO_2 on CuO(110) Surface" *Journal of the Physical Society of Japan*, 84 (2015) 015003.

7. Joaquin Moreno, Susan Aspera, Melanie David, Hideaki Kasai. "A computational study on the effect of local curvature on the adsorption of oxygen on single-walled carbon nanotubes," *Carbon*, 94 (2015) 936-941.

8. Joaquin Lorenzo Valmoria Moreno, Hideaki Kasai. "A DFT study on the adsorption of CO on CuO (110) surface," *Japanese Journal of Applied Physics*, submitted.

9. Joaquin Lorenzo Valmoria Moreno, Allan Abraham Bustria Padama, Hideaki Kasai. "NO reduction and CO oxidation on CuO(110) surface: a density functional theory-based study," *Journal of Physics: Condensed Matter*, submitted.

Presentations in Scientific Meetings

International Conferences:

1. "Density functional theory study of hydrogen peroxide adsorption on pristine and Fe-filled single-walled carbon nanotubes," <u>Joaquin Moreno</u>, Melanie David, Tanglaw Roman, Hideaki Kasai, *The 37th International Symposium on Compound Semiconductors (ISCS 2010)*, May 31 - June 4, 2010, Takamatsu Symbol Tower, Takamatsu, Kagawa, Japan.

2. "DFT study on the adsorption and dissociation of hydrogen peroxide on Fe-filled single-walled carbon nanotubes," <u>Joaquin Moreno</u>, Melanie David, Tanglaw Roman, Mamoru Sakaue, Hideaki Kasai, *2010 International Conference on Solid State Devices and Materials (SSDM-2010)*, September 22-24, 2010, The University of Tokyo, Tokyo, Japan.

3. "A theoretical investigation on the interaction of oxygen with Fe-filled single-walled carbon nanotubes," <u>Joaquin Moreno</u>, Melanie David, Hideaki Kasai, *Workshop on Carbon Nanotube in Commemoration of the 20th Anniversary of its Discovery (2011-CNT20)*, December 12-14, 2011, The International House of Japan, Tokyo, Japan.

4. "DFT-based invetsigations on the interaction of oxygen, hydrogen peroxide, and silicon clusters with single-walled carbon nanotubes," <u>Joaquin Moreno</u>, Melanie David, Mary Clare Escano, Nguyen Tien Quang, Hideaki Kasai, *International Symposium on Carbon Nanotube Nanoelectronics (CNT-NE2012)*, June 11-13, 2012, Nagoya University, Nagoya, Japan.

5. "Theoretical studies on hydrogen and oxygen adsorption on graphene," <u>Joaquin Moreno</u>, Susan Aspera, Melanie David, Tanglaw Roman, Hideaki Kasai, *Graphene Week 2013*, June 2-6, 2013, Technische Universität Chemnitz, Chemnitz, Germany.

6. "DFT study on the interaction of NO and CO with CuO (110) surface," <u>Joaquin Moreno</u>, Allan Padama, Hideaki Kasai, *International Workshop on Atomically Controlled Fabrication Technology*, February 5-6, 2014, Osaka University Nakanoshima Center, Osaka, Japan.

7. "Precious matal-free catalyst for purification of automotive exhausts: NO dissociation on Cu oxide surfaces," Kuniyuki Miwa, Hideaki Kasai, Allan Abraham Padama, <u>Joaquin Lorenzo Moreno</u>, *American Physical Society March Meeting 2014*, March 3-7, 2014,

Colorado Convention Center, Denver, Colorado, USA.

8. "Precious metal free catalyst for exhaust gas purification," Hideaki Kasai, Allan Abraham B. Padama, <u>Joaquin Lorenzo V. Moreno</u>, *2014 Energy Materials Nanotechnology East Meeting*, May 12-15, 2014, Beijing, China.

9. "Designing a precious metal-free catalyst for NO reduction and CO oxidation: The case of CuO (110) surface," <u>Joaquin Moreno</u>, Allan Abraham Padama, Hideaki Kasai, *International Workshop of Computational Nano-Materials Design on Green Energy*, June 1-3, 2014, Osaka University, Osaka, Japan.

10. "Theoretical investigation on copper oxide surfaces as catalyst for automotive exhaust systems," <u>Joaquin Lorenzo Valmoria Moreno</u>, *HeKKSaGOn Summer School 2014*, September 1-10, 2014, Karlsruhe Institute of Technology, Karlsruhe, Germany.

Domestic Conferences:

1. "Adsorption of oxygen and hydrogen peroxide on Pt-decorated and Fe-filled single-walled carbon nanotubes," <u>Joaquin Moreno</u>, Melanie David, Tanglaw Roman, Mamoru Sakaue, Hideaki Kasai, *Carbon Nanotubes Nano-electronics (CNT-NE2010)*, August 2-4, 2010, Nagoya University, Nagoya, Japan.

2. "Selective oxidation of Fe-filled single-walled carbon nanotubes by hydrogen peroxide," <u>Joaquin Moreno</u>, Melanie David, Hideaki Kasai, *15th Osaka University-De La Salle University Academic Workshop*, September 27-30, 2010, De La Salle University, Manila, Philippines.

3. "Density functional theory studies on the adsorption of oxygen and hydrogen peroxide on single-walled carbon nanotubes filled with iron," <u>Joaquin Moreno</u>, Melanie David, Hideaki Kasai, *Carbon Nanotubes Nano-electronics (CNT-NE2011)*, September 14-16, 2011, Tokyo Institute of Technology, Tokyo, Japan.

4. "A DFT study on the adsorption of oxygen and hydrogen peroxide on Fe-filled single-walled carbon nanotubes," <u>Joaquin Moreno</u>, Melanie David, Hideaki Kasai, *4th GCOE on Atomically Controlled Fabrication Technology*, October 31 - November 2, 2011, Osaka University Nakanoshima Center, Osaka, Japan.

5. "DFT-based investigation of hydrogen and oxygen adsorption on graphene," <u>Joaquin Moreno</u>, Susan Aspera, Tanglaw Roman, Melanie David, Hideaki Kasai, *Osaka University-De La Salle University Academic Workshop*, February 12, 2014, De La Salle University, Manila, Philippines.

6. "Interaction of NO and CO with CuO (110) surface," <u>Joaquin Moreno</u>, Hideaki Kasai, *Computational Materials Design Workshop*, February 13-14, 2014, De La Salle University,

Manila, Philippines.

7. "Designing a precious metal-free catalyst for purification of automotive exhausts: NO reduction on various CuO surfaces," <u>Joaquin Moreno</u>, Allan Padama, Hideaki Kasai, *55th Annual Symposium of the Vacuum Society of Japan*, November 18-20, 2014, Osaka Prefectural University I-site Namba, Osaka, Japan.